

AR-009-664

DSTO-TR-0323

A Theoretical Analysis of Target
Tracking in Ground Clutter by
Airborne Pulse Doppler Radars

A P Szabo

DISTRIBUTION STATEMENT R

Approved for public release
Distribution Unlimited

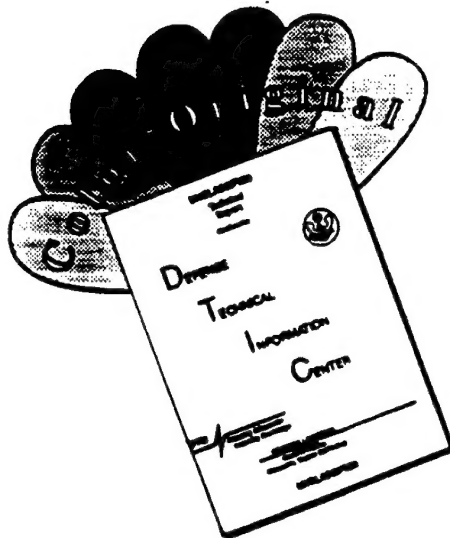
APPROVED FOR PUBLIC RELEASE

© Commonwealth of Australia

19961009 136

DEPARTMENT OF DEFENCE
DEFENCE SCIENCE AND TECHNOLOGY ORGANISATION

DISCLAIMER NOTICE



THIS DOCUMENT IS BEST QUALITY AVAILABLE. THE COPY FURNISHED TO DTIC CONTAINED A SIGNIFICANT NUMBER OF COLOR PAGES WHICH DO NOT REPRODUCE LEGIBLY ON BLACK AND WHITE MICROFICHE.

A Theoretical Analysis of Target Tracking in Ground Clutter by Airborne Pulse Doppler Radars

A. P. Szabo

Electronic Warfare Division
Electronic and Surveillance Research Laboratory

DSTO-TR-0323

ABSTRACT

Target tracking in ground clutter is an important function of airborne pulse Doppler radars. As a tool for analysing the performance of these radars, modifications to an existing computer model of a medium pulse repetition frequency airborne tracking radar have been made to include ground clutter. The clutter signal has been modelled as a Gaussian random field with uncorrelated increments. The field is characterised by the mean clutter power and examples of the mean clutter power are shown for straight and level and diving aircraft. A method of sampling a realisation of the clutter signal in the range-Doppler bins of the radar receiver is described. Examples of the clutter signal are shown for receivers utilising Dolph-Chebyshev weighted Doppler filters and simple pulse train or thirteen bit Barker coded waveforms. The process of pulse repetition frequency selection is considered in detail. Examples of the output from the computer model, both with and without clutter included, are also presented. The results of this analysis show that ground clutter has a significant impact on the way in which target tracking is implemented and needs to be included to accurately model the performance of the radar.

DTIC QUALITY INSPECTED 8

APPROVED FOR PUBLIC RELEASE

DEPARTMENT OF DEFENCE

DEFENCE SCIENCE AND TECHNOLOGY ORGANISATION

APPROVED FOR PUBLIC RELEASE

Published by

*DSTO Electronics and Surveillance Research Laboratory
PO Box 1500
Salisbury South Australia 5108*

*Telephone: (08) 259 5555
Fax: (08) 259 6567
© Commonwealth of Australia 1996
AR-009-664
June 1996*

A Theoretical Analysis of Target Tracking in Ground Clutter by Airborne Pulse Doppler Radars

EXECUTIVE SUMMARY

Target tracking in ground clutter is an important function of airborne pulse Doppler radars. As a tool for analysing the performance of these radars, modifications to an existing computer model of a medium pulse repetition frequency airborne tracking radar have been made to include ground clutter.

The clutter return has been modelled as a Gaussian random process. The model includes the effects of a spherical Earth as well as specular reflections from the Earth's surface. A realistic model of the antenna gain has also been included. An algorithm for calculating the clutter signal in the receiver of an airborne pulse Doppler radar is described. The algorithm includes the effects of the radar signal processing chain on the signal and examples are shown for both simple pulse train and pulse compressed waveforms.

The modification to the existing computer model has required an analysis of the factors which affect the selection of the pulse repetition frequency and the inclusion of pulse repetition frequency selection logic. The automatic gain control model also had to be modified to simulate operation in a clutter environment.

The results of this analysis show that ground clutter has a significant impact on the way in which tracking is implemented in an airborne pulse Doppler radar and needs to be included to accurately model the performance of the radar.

Authors

A. P. Szabo

Electronic Warfare Division

After completing his Ph D in High Energy Astrophysics in 1992, Dr. Szabo was a Research Associate in the Department of Physics and Mathematical Physics at the University of Adelaide where he conducted research into the production of high energy emissions from Active Galactic Nuclei and Supernova Remnants. He joined the Electronic Warfare Division of the Defence Science and Technology Organisation in 1993 and has been undertaking research into advanced countermeasures for airborne pulse Doppler radars. He has also been extensively involved in the activities of TTCP QTP-16 and is a member of the Australian Institute of Physics.

Contents

LIST OF ACRONYMS	XIII
LIST OF SYMBOLS	XV
1. INTRODUCTION	1
2. THE SIGNAL FROM GROUND RETURNS	3
2.1 Calculation of the Mean Clutter Power	4
2.1.1 Antenna Gain	7
2.1.2 The Radar Cross Section of the Earth	10
2.2 Examples of the Mean Clutter Power Received by the Radar	11
3. THE CLUTTER SIGNAL IN THE RADAR RECEIVER	14
3.1 Response of the Radar Receiver in a Ground Clutter Environment	15
3.2 Sampling the Clutter Signal in the Receiver	16
3.3 Implementation Issues	18
3.4 Examples of the Clutter Signal seen by the Radar Receiver	19
4. TARGET DETECTION AND TRACKING IN GROUND CLUTTER	22
4.1 Target Detection	23
4.2 PRF Selection	25
4.2.1 Transmission Blanking and Altitude Line Clearance	25
4.2.2 Mainlobe Clearance	28
4.2.3 Implementation of the PRF selection algorithm	30
4.3 Automatic Gain Control	32
4.4 Modifications to the Model	32
4.5 An Example of Target Tracking in Clutter	33
5. CONCLUSIONS	36
6. ACKNOWLEDGMENTS	36
7. REFERENCES	36

APPENDIX A	TRANSFORMATION MATRICES	39
APPENDIX B	DERIVATION OF THE dA IN TERMS OF R AND v	41
APPENDIX C	MAPPING (R, v) TO (θ, ϕ)	43
APPENDIX D	THE RESPONSE OF THE RADAR	45
APPENDIX E	DOLPH-CHEBYSHEV WEIGHTING	57
Figure 2.1	A schematic diagram showing the reference frames used in calculating the mean clutter power. The platform frame and the antenna frame are shown with their origins offset with respect to the inertial frame for clarity. The inertial frame has its z -axis aligned radially with the centre of the Earth. The platform frame has its x -axis aligned with the velocity of the platform, while the antenna frame has its x -axis aligned with the electrical bore sight of the antenna.	6
Figure 2.2	A plot of the power gain for the sum antenna pattern used in this analysis. The variables y_a and z_a are direction cosines in the plane of the array and are given in terms of θ and ϕ by Equations 2.9 and 2.10. The antenna pattern shown here has a nominal beamwidth of 3.3° and the array has been Dolph-Chebyshev weighted in an attempt to produce sidelobes 55 dB down relative to the mainlobe.	8
Figure 2.3	A plot of the power gains for the difference antenna patterns used in this analysis. Variables and parameters are the same as for Figure 2.2.	9
Figure 2.4	The mean radar cross section model used in this analysis. Specular reflection can be seen to dominate for angles close to 90° while the diffuse component dominates else where.	10
Figure 2.5	Mean clutter power as seen by an aircraft flying straight and level with a velocity of 300 ms^{-1} at an altitude of 5000 m. The antenna has an elevation of -45° and an azimuth of 45° . The yellow ellipse at a Doppler shift of 10 kHz is the mainlobe contribution. The ripple effect from the sidelobes of the antenna pattern is also clearly seen.	11

Figure 2.6	Mean clutter power as seen by an aircraft at an altitude of 1000 m when in a 45° dive. As before the aircraft's velocity is 300 ms ⁻¹ , however the elevation of the antenna is now 30°. The mainlobe contribution forms the long bar at approximate 15 kHz. The contribution from the antenna sidelobes can again be clearly seen, although now the boundary of the sidelobe contribution is asymmetric. This asymmetry is caused by the aircraft diving.	12
Figure 3.1	The folded mean clutter power corresponding to mean clutter power shown in Figure 2.5. Aircraft parameters are as for Figure 2.5 and we have used a PRF of 15.625 kHz.	19
Figure 3.2	A realisation of the folded clutter signal which has the mean clutter power shown in Figure 3.1.	20
Figure 3.3	An example of the clutter signal seen in a radar receiver utilising a simple pulse train with a Dolph-Chebyshev weighted matched filter. Here we have used 64 range bins, of length 1 µs or 150 m, along with 32 Doppler filters.	20
Figure 3.4	Another realisation of the folded clutter signal with mean clutter power shown in Figure 2.5. Here we have used PRI of 128 µs, which corresponds to an unambiguous range of 19,200 m, and a PRF of 7.8125 kHz. Notice that the transmission blanking require for a 13 bit Barker coded waveform is considerably longer than for the simple pulse train and occupies nearly 2000 m of the unambiguous range interval. The range and Doppler scales have the same relative proportions as used in Figure 3.2 to emphasize the change in the shape of the unambiguous range-Doppler interval with PRF.	21
Figure 3.5	An example of the clutter signal seen by a radar receiver utilising a thirteen bit Barker coded pulse train with a Dolph-Chebyshev weighted low pass filter. Here we have used 128 range bins, of length 1 µs or 150 m, along with 32 Doppler filters.	21
Figure 4.1	A schematic diagram showing the main features on the unambiguous range-Doppler interval. Here we have notionally shown two of the medium PRFs, (a) and (b), to demonstrate how the dimensions of the unambiguous range-Doppler interval and the position of the target and clutter can change with PRF. A hypothetical example of the range-Doppler bins which could be used for CFAR processing are also shown.	24

Figure 4.2	A plot of the PRI bands which satisfy the range clearance criteria (Equation 4.1) for an aircraft flying at an altitude of 5000 metres. The red shaded bands are formed by PRIs which put the target after the altitude line and before the next blanking pulse. The blue shaded bands are formed by PRIs which put the target before the altitude line	27
Figure 4.3	A plot of the PRI bands which satisfy the range clearance criteria (Equation 4.1) for an aircraft flying at an altitude of 1000 metres. Bands are defined as for Figure 4.1.	28
Figure 4.4	A plot of the PRI bands (red shaded regions) which satisfy the Doppler clearance criteria (Equation 4.9) as a function of the relative Doppler shift, i.e. the difference between the target Doppler shift and the mainlobe clutter frequency, for $v_o = 500$ Hz.	30
Figure 4.5	A plot of the PRI bands (red shaded regions) which satisfy the Doppler clearance criteria (Equation 4.9) as a function of the relative Doppler shift, i.e. the difference between the target Doppler shift and the mainlobe clutter frequency, for $v_o = 2500$ Hz.	31
Figure 4.6	A plot of some of the output from the computer model when ground clutter is not included. See text for a description of the scenario. Shown are (a) target signal to noise ratio, and the (b) range and (c) Doppler discriminants (solid line). The bounds on the discriminants (dotted line), based on the range and Doppler residuals, are also shown.	34
Figure 4.7	A plot of some of the output from the computer model when ground clutter is included. See text for a description of the scenario. Shown are (a) target signal to noise ratio, and the (b) range and (c) Doppler discriminants (solid line). The bounds on the discriminants (dotted line), based on the range and Doppler residuals, are also shown.	35
Figure B.1	A schematic diagram of the inertial frame and the Earth.	41
Figure D.1	The ambiguity function, $\chi_{\mu\mu}(\tau, \nu)$, of a rectangular pulse with a duration of $1 \mu\text{s}$.	48
Figure D.2	The cross ambiguity function, $\chi_{sf}(\tau, \nu)$, of a simple pulse train and a Dolph-Chebyshev weighted matched filter. Here we have used a PRI of $64 \mu\text{s}$ which corresponds to a PRF of 15.625 kHz and we have generated 32 Doppler filters.	49
Figure D.3	A close up in the region near $\tau = 0$ and $\nu = 0$ of the cross ambiguity function shown in Figure D.2.	50

- Figure D.4 A close up of the cross ambiguity function in the region near $\tau = 0$ and $\nu = 0$ for a simple pulse train and a Dolph-Chebyshev weighted low pass filter. Again we have $T_p = 1 \mu\text{s}$, $T_r = 64 \mu\text{s}$ and $N = 32$. 51
- Figure D.5 A close up of the cross ambiguity function in the region near $\tau = 0$ and $\nu = 0$ for a thirteen bit Barker coded pulse train and a Dolph-Chebyshev weighted matched filter. Again we have $T_p = 1 \mu\text{s}$, $T_r = 64 \mu\text{s}$ and $N = 32$. 53
- Figure D.6 A close up of the cross ambiguity function in the region near $\tau = 0$ and $\nu = 0$ for a thirteen bit Barker coded pulse train and a Dolph-Chebyshev weighted low pass filter. Again we have $T_p = 1 \mu\text{s}$, $T_r = 64 \mu\text{s}$ and $N = 32$. 54

List of Acronyms

ADC	Analogue to Digital Converter
AGC	Automatic Gain Control
APDR	Airborne Pulse Doppler Radar
CACFAR	Cell Averaged Constant False Alarm Rate
CFAR	Constant False Alarm Rate
DFT	Discrete Fourier Transform
ECM	Electronic Countermeasure
FFT	Fast Fourier Transform
GMT	Ground Moving Target
GOCFAR	Greatest Of Constant False Alarm Rate
IF	Intermediate Frequency
MLC	Main Lobe Clutter
MPRF	Medium Pulse Repetition Frequency
PRF	Pulse Repetition Frequency
PRI	Pulse Repetition Interval
RCS	Radar Cross Section
RF	Radio Frequency
SOCFAR	Smallest Of Constant False Alarm Rate
SNR	Signal to Noise Ratio

List of Symbols

A	average target power
α	angle between \vec{r} and \vec{v}
a_r	amplitude of returned signal
$a_T(t)$	amplitude of target return
$\chi_{ss}(\tau, \nu)$	ambiguity function of the signal transmitted by the radar
$\chi_{rs}(\tau, \nu)$	cross ambiguity function of the signal received by the radar and the transmitted signal
$\chi_{\mu\mu}(\tau, \nu)$	ambiguity function of the envelopes of the individual pulses in the pulse train
$\chi_{sj}(\tau, \nu)$	cross ambiguity function of the transmitted signal and the reference signal
$\chi_{rj}(\tau, \nu)$	cross ambiguity function of the received signal and the reference signal
$\delta(\cdot)$	Dirac delta function
dA	incremental area on the Earth's surface
$dc(R, \nu)$	mean clutter power per unit area measured in the RF portion of the radar prior to amplification or processing
$dZ(R, \nu)$	an increment of the random clutter field $Z(R, \nu)$
$dZ_{\Sigma}(R, \nu)$	an increment of the random clutter field when the contributions from the ambiguous ranges and Doppler shifts have been folded in
$\Delta\nu_{MLC}$	width of mainlobe clutter in the Doppler domain
ΔR	range bin width
E	total energy of the waveform
f	frequency of the RF carrier
F	factor which determines the probability of signal clipping in the ADC
$F(R, \nu)$	geometrical function used to map the Earth's surface in terms of R and ν .
ϕ	angle between the projection of \vec{r} onto the $y_a z_a$ -plane, and the y_a -axis
φ	angle between \vec{r} and the local tangent to the Earth's surface
φ_o	angular width of the specular component of the mean RCS of the Earth
$G_R(\theta, \phi)$	antenna gain when receiving radiation
$G_T(\theta, \phi)$	antenna gain when transmitting radiation
γ	angle between \vec{r} and the z -axis
h	altitude of the aircraft
$I(t, f)$	intensity of the signal $\psi(t)$
k_o	minimum number of range bins the transmission blanking pulse must precede the target by to avoid corrupting the target bins or the range CFAR bins

k_1	minimum number of range bins the transmission blanking pulse must lag the target by to avoid corrupting the target bins or the range CFAR bins
l_0	minimum number of range bins the altitude line must proceed the target by to avoid corrupting the target bins or the range CFAR bins
l_1	minimum number of range bins the altitude line must lag the target by to avoid corrupting the target bins or the range CFAR bins
λ	wavelength of the radar's RF carrier
$\mu(t), \mu'(t)$	envelope of the individual pulses in the pulse train
$M(f)$	spectral density of $\mu(t)$
$n(t)$	zero mean white noise process
N	number of pulses in the radar pulse train
N_{rb}	number of range bins per PRI
N_o	spectral density of the zero mean white noise process
v	Doppler shift of the point \vec{r} on the Earth's surface
v_{\max}	maximum possible Doppler shift of ground returns
$v_{\min}(R)$	minimum Doppler shift of the ground returns as a function of range
$v_{\max}(R)$	maximum Doppler shift of the ground returns as a function of range
v_o	minimum separation between the target Doppler shift and the MLC frequency to avoid corrupting the target bins or the Doppler CFAR bins
v_u	unambiguous Doppler shift of the radar waveform (corresponds to one PRF)
v_{offset}	Doppler offset designed to bring the ambiguous MLC frequency directly below the target Doppler shift to zero hertz
v_{GMT}	Doppler threshold for ground moving targets
v_T	target Doppler shift
v_{MLC}	mainlobe clutter frequency
P_T	peak transmitter power of the radar
$\psi_f(t)$	radar receiver's reference signal expressed in complex form
$\psi_s(t)$	radar's transmitted signal expressed in complex form
$\psi_r(t)$	received signal expressed in complex form
$\Psi(f)$	spectral density of the signal $\psi(t)$
$\vec{r} = (x, y, z)$	vector to a point on the Earth's surface, resolved in the inertial frame
$R = \vec{r} $	range to a point \vec{r} on the Earth's surface
$\vec{r}_a = (x_a, y_a, z_a)$	vector to a point on the Earth's surface, resolved in the antenna frame
$\vec{r}_p = (x_p, y_p, z_p)$	vector to a point on the Earth's surface, resolved in the platform frame
R_E	mean radius of the Earth
R_{MLC}	range to mainlobe clutter
R_u	unambiguous range of the radar waveform
$r(t)$	signal received by the radar
$s(t)$	signal transmitted by the radar

$\sigma(\varphi)$	mean RCS of the Earth's surface
σ_d	scaling factor for the diffuse component of the mean RCS of the Earth
σ_s	scaling factor for the specular component of the mean RCS of the Earth
ζ_p	roll angle of the aircraft
θ	angle between \vec{r} and the x_a -axis
θ_o	3 dB beamwidth of the antenna
T_p	pulse duration
T_r	pulse repetition interval
$T_x(\zeta)$	transformation matrix for a rotation through angle ζ about the x-axis
$T_y(\zeta)$	transformation matrix for a rotation through angle ζ about the y-axis
$T_z(\xi)$	transformation matrix for a rotation through angle ξ about the z-axis
$T_m(u)$	Chebyshev polynomial of degree m
τ	two way signal delay corresponding to a range R
τ_T	target delay
τ_u	unambiguous delay of the radar waveform (corresponds to one PRI)
\vec{v}	velocity vector of the aircraft
V	magnitude of the largest number which can be stored in the bulk memory of the radar
w_n	sequence of weights for the pulses in the pulse train
ξ_a	azimuth angle of the antenna
ξ_p	yaw angle of the aircraft
ζ_a	elevation angle of the antenna
ζ_p	pitch angle of the aircraft

1. Introduction

In this report we will be principally concerned with an analysis of the performance of the medium pulse repetition frequency (MPRF) tracking mode of airborne pulse Doppler radars (APDRs). This has involved the development of a high fidelity model of a generic APDR and the implementation of the model in SUN FORTRAN for use in various studies. The model of the radar did not include any representation of clutter, and a natural development of this work is the investigation of how ground clutter affects the ability of an APDR to track a target.

The question of how ground clutter affects APDRs has been analysed by a number of authors in the open literature. Farrell and Taylor (1964) are amongst the first to publish a computation of the clutter spectrum for an APDR. However, they made a number of simplifying approximations including the requirement that the antenna is spherically symmetric and has a beam width less than 15°. Many of these approximations were addressed by Friedlander and Greenstein (1970). They described a computerised procedure for calculating the clutter power in the range-Doppler processing cell for a general antenna pattern, pulse shape, clutter reflectivity and pulse repetition frequency (PRF). They also included the effects of a spherical Earth and the radar signal processing on the clutter power. A number of other authors (e.g. Ringel 1977, Mitchell 1978, Sandhu 1981, Jao and Goggins 1985) have since performed calculations in an attempt to create a high fidelity model of the ground clutter seen by APDRs which can be calculated in real time. Unfortunately the complexity of the problem means that all of the authors have been forced to make some approximations.

The calculation of the ground clutter seen by an APDR presented in this report differs from those presented in the literature in a number of important ways. The generic APDR model does not run in real time and so the constraint on the clutter calculation to be performed in real time is relaxed. Despite this, it is still important for the calculation to be efficient as it is envisaged the model will be used for Monte Carlo type calculations. While the clutter is modelled as a Gaussian random field for the analysis presented in this report, the calculation has been kept general enough so that other statistical models of the clutter field could readily be accommodated. The computation procedure of Friedlander and Greenstein 1969 has also been further generalised so that the transmission and reception antenna patterns may be different. This has been done so that the signal in the sum and difference channels of the receiver can be easily calculated.

Another key difference is that the clutter return has been modelled statistically *and* the phase information has been maintained throughout the calculation of the signal in the radar receiver. The result is that we calculate the field strength in the range-Doppler bins rather than just the mean clutter power in the bins. This has been done so that the correlations between range-Doppler processing bins have been calculated

correctly. This is important because APDRs generally make use of the phase information in the signal during processing and hence an accurate representation of the clutter signal is required to be able to gauge the effect of ground clutter on the receiver.

As we shall see later in this report, the main clutter features which impact on the processing in the receiver in MPRF modes are mainlobe clutter and altitude line. Mainlobe clutter returns result from the mainlobe of the antenna illuminating the Earth and may be more than 30 dB above the returns from the sidelobe, depending on the antenna's mainlobe to sidelobe ratio. The altitude line results from specular reflections from the ground directly below the aircraft and may occur even when the mainlobe is not illuminating the Earth. The detection performance of the radar decreases when the target is obscured by these features as they elevate the background signal the target has to compete with. The receiver minimises the impact that mainlobe clutter and altitude line have on radar performance by selecting the PRF so that the target is not corrupted by these features. This allows the radar to perform target tracking in MPRF mode as the target has to compete only with returns from the sidelobe of the antenna.

A number of changes were required to include ground clutter in the computer model of MPRF mode. The most significant of these changes were the routines which calculate the mean clutter power in the radar receiver and sample a realisation of the clutter signal in the receiver. However, routines for selecting the PRF also had to be added and this required a detailed analysis of the selection logic. A routine for simulating the receiver's automatic gain control in a clutter environment was also added. Examples of the output from the computer model both with and without clutter are presented in this report for a typical target track. However no attempt is made to provide a detailed analysis of the effectiveness of MPRF mode in a broad range of operational scenarios.

This report has been organised as follows. The characterisation of the ground return in terms of a zero mean complex Gaussian random process is described in Section 2. A key ingredient in this model is the mean clutter power and this is described in detail here. The results from Sections 2 are used in Section 3 to calculate the range-Doppler clutter signal in the radar receiver. Two methods of sampling a realisation of the clutter signal in the radar receiver are also described along with details of how the clutter sampling algorithm was implemented. Target detection and PRF selection in MPRF mode are discussed in Section 4, along with a description of how the existing model had to be modified to include ground clutter. Track performance, both with and without ground clutter, is also discussed. The conclusions are presented in Section 5.

2. The Signal from Ground Returns

The signal reflected from the Earth when it is illuminated by a radar is generally made up of two contributions, a return from the resolvable discrete scatterers on the Earth's surface and a diffuse return. The presence and the spatial distribution of resolvable discrete scatterers is highly dependent on the terrain and the inclusion of discrete sources would make the analysis presented here less general. Hence, in this report we shall concern ourselves principally with the diffuse return from the Earth. This component also forms the majority of the background in which APDRs have to operate and so impacts strongly on the signal processing of APDRs. If discrete scatterers are required for some future work then they can simply be added in much the same way as discrete targets.

The diffuse component of the radar return can be thought of as being composed of the linear supposition of the returns from unresolvable discrete scatterers on the Earth's surface. The reflected signal can therefore be characterised by the statistics of the unresolved discrete scatterers. In this report the clutter signal from ground returns will be modelled as a Gaussian random field. This is justified by invoking the Central Limit Theorem as follows. Consider an area of the Earth's surface (a patch) which contains a number of the unresolved discrete scatterers. The return from each of these scatterers will have a random amplitude and phase. The Central Limit Theorem says that if we take the sum of several random variables then the distribution of the sum will approach a Gaussian distribution, independent of the distributions of the individual random variables. Hence, so long as the number of unresolved discrete scatterers in the patch is not too small, the signal from the patch can be well approximated by a Gaussian random process.

What of the spatial distribution of these unresolved discrete scatterers? We shall assume here that the scatterers are uniformly distributed on the Earth's surface. The degree of correlation in the signals from the unresolved scatterers will be dependent on the length scale considered. For example one can imagine that the return from a feature on the Earth's surface, such as a rocky outcrop or a pond, will be highly correlated on length scales similar to the size of the feature. Hence, so long as the patch of ground we are considering is larger than the typical length scale of features on the Earth's surface then the signal from neighbouring patches will be completely uncorrelated.

Let the clutter signal be represented by a two dimensional Gaussian random field $Z(R, \nu)$, where we have mapped the Earth's surface in terms of the range, R , and Doppler shift, ν , measured with respect to the APDR. If the signal is spatially uncorrelated as described above then this means that the increments, $dZ(R, \nu)$, of the random field are uncorrelated. Mathematically this is represented by the covariance of the field taking the form

$$\left\langle dz(R_1, v_1) \overline{dz(R_2, v_2)} \right\rangle = dc(R_1, v_1) \delta(R_1 - R_2) \delta(v_1 - v_2), \quad (2.1)$$

where $dc(R, v)$ is the mean power returned from an incremental patch of ground, $dRdv$, and $\delta(\cdot)$ is the Dirac delta function. Here the angled brackets indicate the use of the expectation operator.

In the above we have considered only the spatial distribution of the clutter signal. What of the temporal distribution? We will assume that the clutter return is uncorrelated on time scales in the order of the coherent integration time of the MPRF mode of APDRs. This means that a realisation of the clutter signal sampled during any coherent integration period will be independent of all other realisations of the clutter signal. Physically this is reasonable since the coherent integration time in MPRF mode is of the order of 5 ms which is much shorter than the time scales on which one might imagine the return from the Earth's surface changing due to things such as trees swaying in the breeze.

This model will be appropriate so long as the patch of ground is not made too small. In this model the clutter signal is completely characterised by $dc(R, v)$ and much of the rest of this section is devoted to deriving an expression for the mean clutter power. Two examples of the mean clutter power used in this model along with formulae characterising the main features of the mean clutter power are also presented in this section.

2.1 Calculation of the Mean Clutter Power

Consider an aircraft flying at a height, h , and with a velocity, \vec{v} , in the inertial reference frame, as shown in Figure 2.1. The inertial reference frame is defined so that the z -axis is pointing at the centre of the Earth and the origin of the reference frame is a distance h above the Earth's surface. The platform frame is given by rotating the inertial frame through an angle ξ_p about the z -axis (yaw), followed by a rotation through angle ζ_p about the y -axis (pitch) and finally a rotation through angle ς_p about the x_p -axis (roll), aligning the x_p -axis with the aircraft's velocity vector. All of the rotations are in clockwise direction when looking along the axis of rotation. Clearly the diffuse clutter signal received by the radar will be not be dependent on the yaw angle of the aircraft because we have assumed that the discrete scatterers are uniformly distributed on the Earth's surface. Hence the yaw of the aircraft is set to zero in the rest of the analysis presented here without any loss of generality. The antenna frame is similarly given by rotating the platform frame through an angle ξ_a about the z_p -axis (antenna azimuth) followed by a rotation through angle ζ_a about the y_p -axis (antenna elevation), aligning the x_a -axis with the electrical bore sight of the antenna. The matrices which are required for transformations between the inertial, platform and antenna frames are derived in Appendix A.

Let the vector $\vec{r} = (x, y, z)$ represent a point on the Earth's surface resolved in the inertial frame (see Figure 2.1) and let R be the range from the aircraft to that point. If

the radar on board the aircraft transmits with a power, P_T , then the average power returned by a patch of ground with area dA at a range R , measured at RF prior to amplification or processing, is given by (see e.g. Friedlander and Greenstein 1970)

$$dc = \frac{P_T \lambda^2 G_T(\theta, \phi) G_R(\theta, \phi) \sigma(\phi)}{(4\pi)^3 R^4} dA. \quad (2.2)$$

Here λ is the wavelength of the RF carrier, $G_T(\theta, \phi)$ is the gain of the antenna during transmission, $G_R(\theta, \phi)$ is the gain of the antenna during reception and $\sigma(\phi)$ is the mean radar cross section (RCS) per unit area of the ground being illuminated. Here, the antenna gains during transmission are shown explicitly as we will require the clutter signal in both the sum and difference channels of the APDR. The angle θ , ϕ and φ are defined in Figure 2.1. The area dA can be expressed in terms of range and Doppler shift as (Friedlander and Greenstein 1970)

$$dA = \frac{RR_E}{(R_E + h)} \frac{dR dv}{v_{\max} F(R, v)} \quad (2.3)$$

where R_E is the radius of the Earth and

$$v_{\max} = \frac{2v}{\lambda} \quad (2.4)$$

is the maximum possible value of the Doppler shift. A derivation of Equation 2.3 can also be found in Appendix B. The Doppler shift of a point \vec{r} which forms an angle α with the velocity \vec{v} , as shown in Figure 2.1, is given by

$$v = \frac{2v \cos \alpha}{\lambda}. \quad (2.5)$$

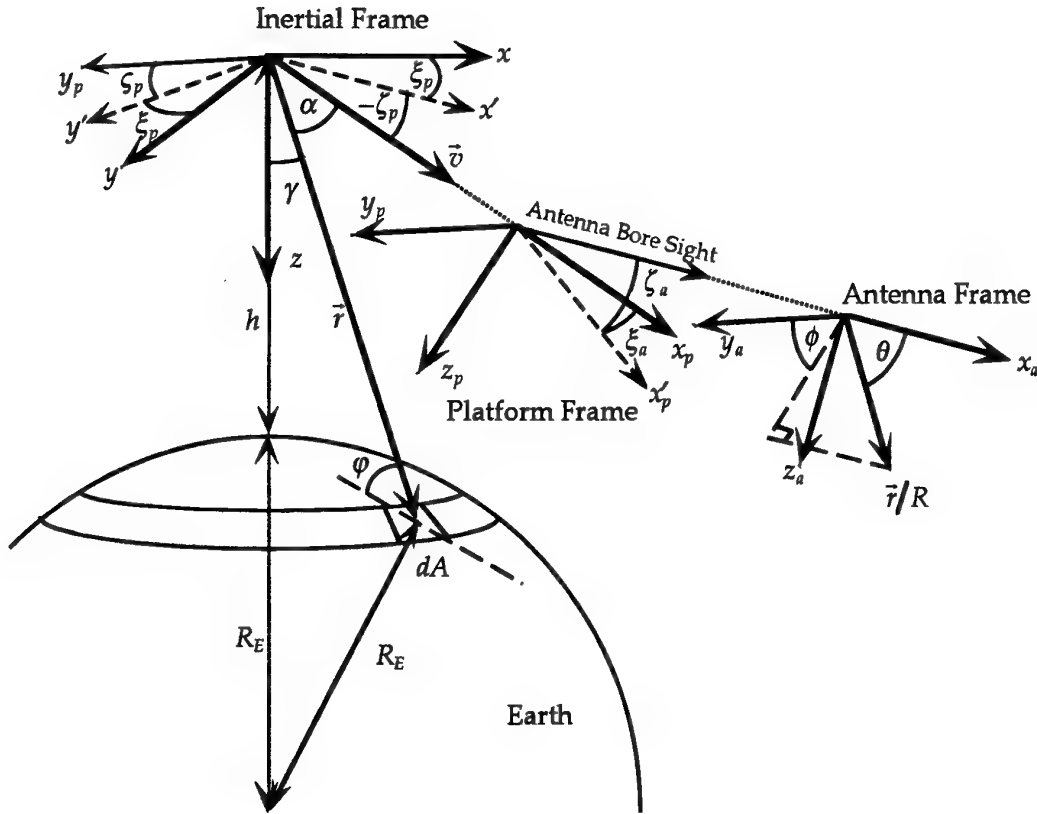


Figure 2.1 A schematic diagram showing the reference frames used in calculating the mean clutter power. The platform frame and the antenna frame are shown with their origins offset with respect to the inertial frame for clarity. The inertial frame has its z -axis aligned radially with the centre of the Earth. The platform frame has its x -axis aligned with the velocity of the platform, while the antenna frame has its x -axis aligned with the electrical bore sight of the antenna.

From Equation 2.5 we can see that v_{\max} corresponds to the case where $\cos\alpha = 1$, i.e. the point lies in the direction of the platform's velocity vector. The function,

$$F(R, v) = \sqrt{\cos^2 \zeta_p - \cos^2 \alpha - \cos^2 \gamma - 2 \cos \alpha \sin \zeta_p \cos \gamma}, \quad (2.6)$$

shown in Equation 2.3 is a geometrical function which arises from mapping the Earth's surface in terms of R and v . Here γ is the angle between \vec{r} and the z -axis of the inertial frame and is given by

$$\cos \gamma = \frac{h}{R} + \frac{R^2 - h^2}{2R(R_E + h)}. \quad (2.7)$$

The second term on the right hand side of Equation 2.7 may be ignored for APDR applications except when the platform flies at very low altitudes and so Equation 2.6 can be approximated as

$$F(R, \nu) \approx \sqrt{\cos^2 \zeta_p - \frac{\nu^2}{\nu_{\max}^2} - \frac{h^2}{R^2} - 2 \frac{\nu}{\nu_{\max}} \frac{h}{R} \sin \zeta_p} \quad (2.8)$$

which shows the dependence on range and Doppler shift more clearly.

2.1.1 Antenna Gain

Modern APDRs typically use planar array antennas with some form of monopulse processing to effect angle tracking. Planar arrays are used because they allow the gain of the antenna to be tailored to reduce the level of the sidelobes. The power gain for the antenna sum pattern used in this study is shown in Figure 2.2. Here we have plotted the antenna gain in terms of direction cosines in the plane of the array

$$y_a = \sin \theta \cos \phi \quad (2.9)$$

$$z_a = \sin \theta \sin \phi, \quad (2.10)$$

and so the electrical bore sight ($\theta = 0$) corresponds to $(y_a, z_a) = (0, 0)$. For the antenna modelled here, the elements of the array form a rectangular grid and have been Dolph-Chebyshev weighted so as to produce uniform sidelobes down 55 dB in power relative to the mainlobe. However, from Figure 2.2 we can see that, while the sidelobes are reasonably uniform, the first sidelobe is only down by about 36 dB. The degradation in the pattern comes chiefly from using a rectangular grid array with a circular boundary. Similar degradation is likely to occur with a real array and hence this antenna pattern will be adequate for our needs in this analysis. The difference patterns of the antenna model are shown in Figure 2.3.

To be able to use the model of the antenna gain to evaluate Equation 2.2 we need to be able to transform from (R, ν) coordinates to (θ, ϕ) coordinates. The transformation required to achieve this is derived in Appendix C.

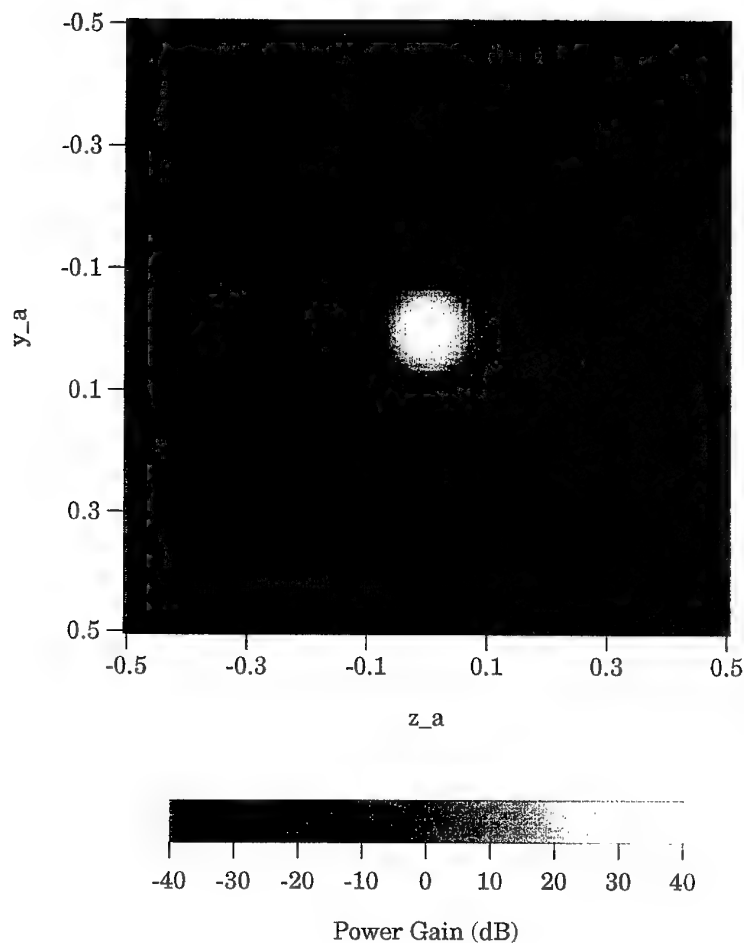


Figure 2.2 A plot of the power gain for the sum antenna pattern used in this analysis. The variables y_a and z_a are direction cosines in the plane of the array and are given in terms of θ and ϕ by Equations 2.9 and 2.10. The antenna pattern shown here has a nominal beamwidth of 3.3° and the array has been Dolph-Chebyshev weighted in an attempt to produce sidelobes 55 dB down relative to the mainlobe.

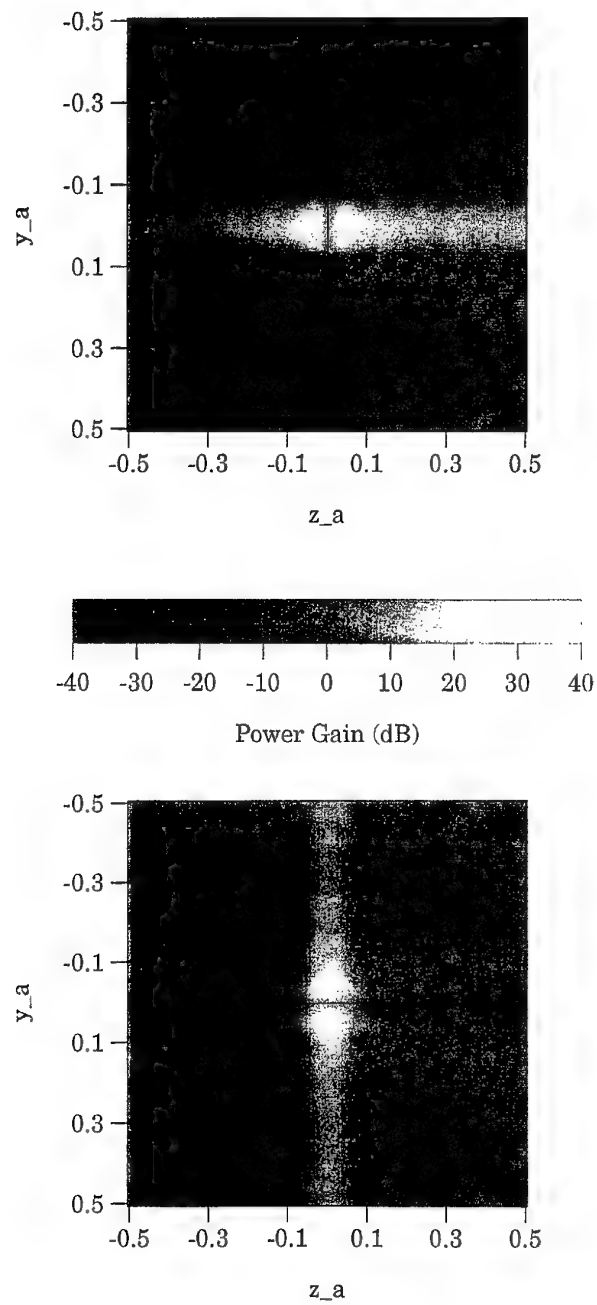


Figure 2.3 A plot of the power gains for the difference antenna patterns used in this analysis. Variables and parameters are the same as for Figure 2.2.

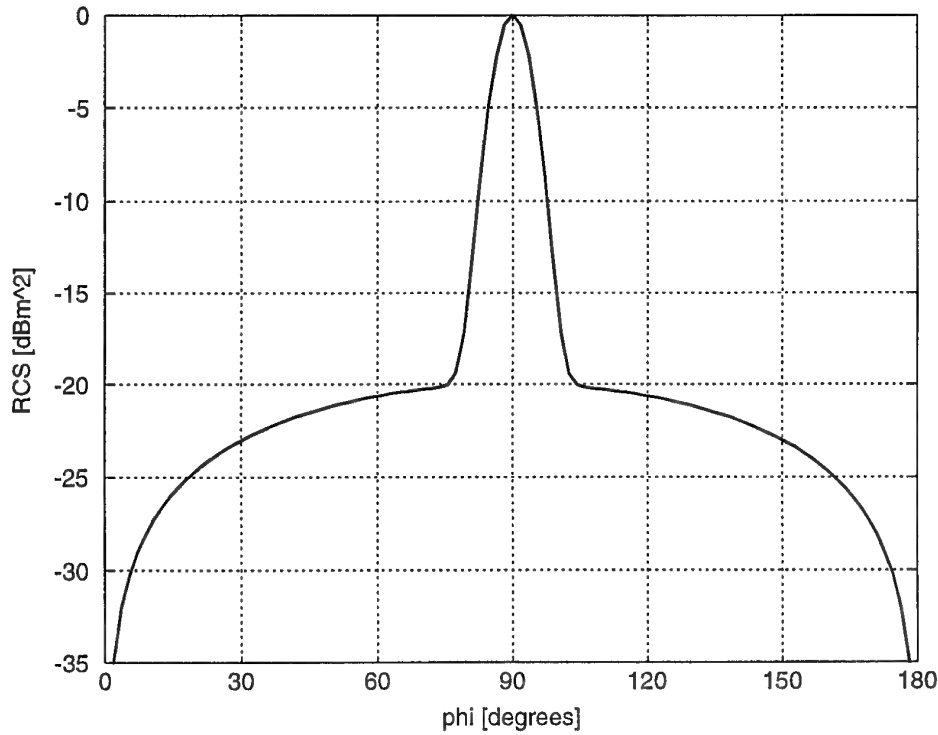


Figure 2.4 The mean radar cross section model used in this analysis. Specular reflection can be seen to dominate for angles close to 90° while the diffuse component dominates elsewhere.

2.1.2 The Radar Cross Section of the Earth

The mean radar cross section of the Earth may be modelled as consisting of two components, a specular component and a diffuse component. The specular component dominates when the incident radiation is almost normal to the Earth surface. The mean RCS used in this report is given by (see e.g. Mitchell 1978)

$$\sigma(\varphi) = \sigma_d \sin \varphi + \sigma_s e^{-|\pi/2 - \varphi|^2 / \varphi_o^2}, \quad (2.11)$$

where σ_d is the RCS of the diffuse component, σ_s is the RCS of the specular component and φ_o is the angular width of the specular component. The mean RCS is shown in Figure 2.4 for $\sigma_d = 0.01 \text{ m}^2$, $\sigma_s = 1 \text{ m}^2$ and $\varphi_o = 5^\circ$.

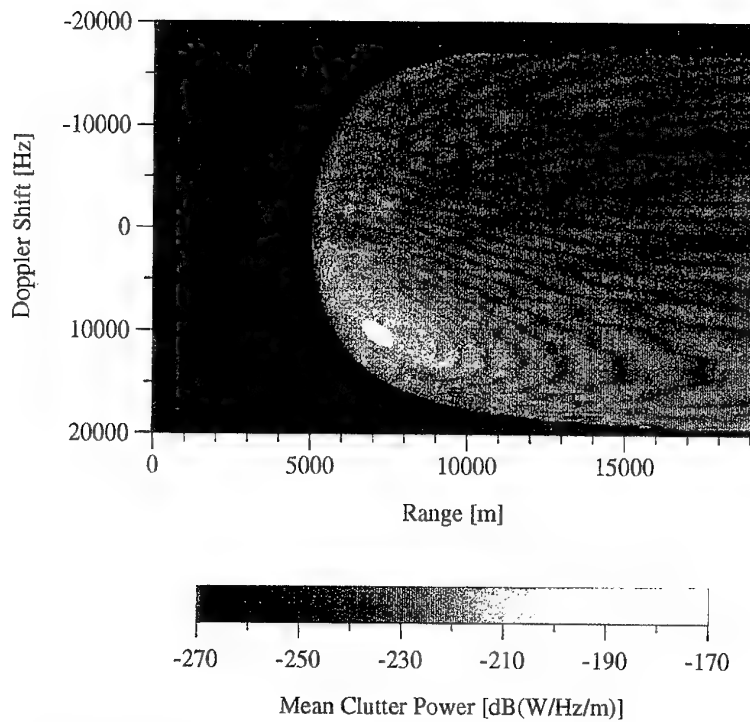


Figure 2.5 Mean clutter power as seen by an aircraft flying straight and level with a velocity of 300 ms^{-1} at an altitude of 5000 m. The antenna has an elevation of -45° and an azimuth of 45° . The yellow ellipse at a Doppler shift of 10 kHz is the mainlobe contribution. The ripple effect from the sidelobes of the antenna pattern is also clearly seen.

2.2 Examples of the Mean Clutter Power Received by the Radar

An example of the mean clutter power from ground returns (Equation 2.2) is shown in Figure 2.5. Here we have used a transmitter with a peak power of 1.5 kW and a wavelength of 3 cm, on an aircraft flying at an altitude of 5 km with zero pitch and roll and a velocity of 300 ms^{-1} . The antenna has an elevation angle of -45° and an azimuth of 45° . From Figure 2.5 we can see that the return can be characterised by contributions from the mainlobe and the sidelobes of the antenna pattern. In this case the mainlobe forms an ellipse on the range-Doppler plane, however as the mainlobe moves towards the radar horizon the mainlobe contribution forms a long narrow bar as shown in Figure 2.6. Here the parameters are as before except that aircraft is now flying at an altitude of 1 km in a 45° dive (still with zero roll) and the antenna's elevation is 30° .

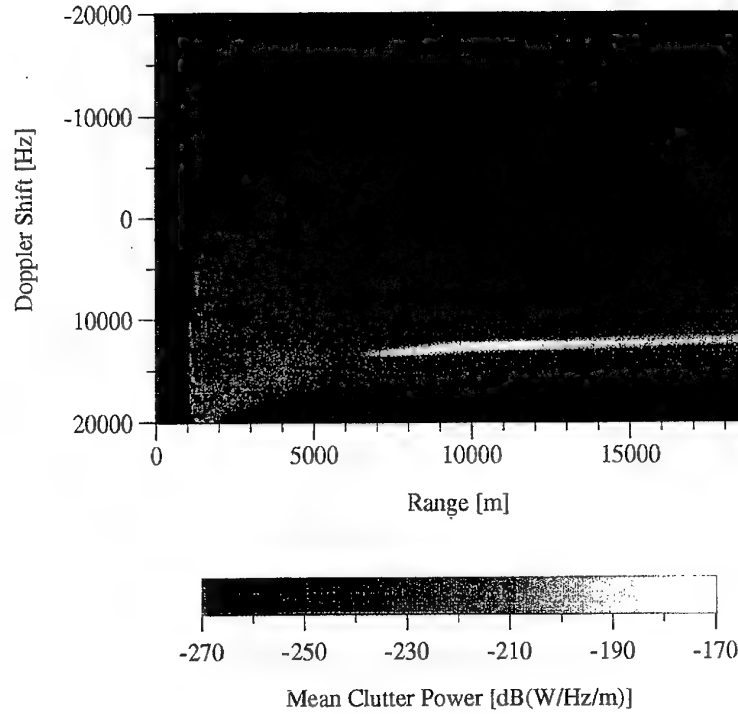


Figure 2.6 Mean clutter power as seen by an aircraft at an altitude of 1000 m when in a 45° dive. As before the aircraft's velocity is 300 ms^{-1} , however the elevation of the antenna is now 30° . The mainlobe contribution forms the long bar at approximate 15 kHz. The contribution from the antenna sidelobes can again be clearly seen, although now the boundary of the sidelobe contribution is asymmetric. This asymmetry is caused by the aircraft diving.

At what range and Doppler shift do we expect mainlobe clutter contributions? To answer this question we need to be able to transform from (θ, ϕ) coordinates to (R, v) coordinates. The transformations required to achieve this are derived in Appendix C. The Doppler shift on which the mainlobe contribution is centred can be calculated by substituting $\theta = \phi = 0$ into Equation C.8 for $\cos \alpha$, and then substituting into Equation 2.5 to give

$$v_{MLC} = v_{\max} \cos \xi_a \cos \zeta_a. \quad (2.12)$$

Similarly, the range on which the mainlobe contribution is centred is given by solving Equation C.2 for R yielding

$$R_{MLC} = (R_E + h) \cos \gamma \pm \sqrt{(R_E + h)^2 \cos^2 \gamma - h(2R_E + h)}. \quad (2.13)$$

Here $\cos\gamma$ is evaluated by rearranging Equation C.10 and substituting $\theta = \phi = 0$. For the example shown in Figure 2.5 we would expect the mainlobe to be centred on a range of 7073 m and a Doppler shift of 10 kHz.

The width of the mainlobe contribution in the Doppler domain, as long as all of the antenna's mainlobe is illuminating the ground, can be calculated by substituting the antenna beamwidth ($\theta = \theta_o$) into Equation C.8 for $\cos\alpha$ and differentiating with respect to ϕ . Solving for the stationary points gives the values of ϕ which yield the maximum and minimum Doppler shifts in the return from the mainlobe. Following this procedure we find that, when neither the antenna azimuth or elevation are zero, i.e. $\zeta_a \neq 0$ and $\xi_a \neq 0$, the maximum and minimum Doppler shifts in the mainlobe occur for $\tan\phi = \sin\zeta_a / \tan\xi_a$. By substituting ϕ and $(\phi + \pi)$ into Equation C.8 and then substituting into Equation 2.5 the width of the mainlobe in the Doppler domain can be expressed as

$$\Delta v_{MLC} = 2v_{\max} \left| \frac{\sin\theta_o \cos\phi}{\sin\xi_a} \left[\sin^2\xi_a + \sin^2\zeta_a \cos^2\xi_a \right] \right|. \quad (2.14)$$

For the example shown in Figure 2.5 and using an antenna with a beamwidth of 3.3° we would expect the mainlobe to be approximately 2 kHz wide. When the antenna has zero azimuth angle ($\xi_a = 0$) but a non-zero elevation angle ($\zeta_a \neq 0$) then Equation 2.14 reduces to

$$\Delta v_{MLC} = 2v_{\max} |\sin\theta_o \sin\zeta_a|. \quad (2.15)$$

The width of the mainlobe in the Doppler domain never goes to zero as is implied by Equation 2.15 because of the inherent beam width of the antenna. Hence when the azimuth angle and the elevation angle of the antenna both tend to zero the width of the mainlobe in the Doppler domain tends to $\Delta v_{MLC} = v_{\max}(1 - \cos\theta_o)$.

We can, in principle at least, calculate the extent of the mainlobe contribution to the mean clutter power in the range domain in a similar way as for the Doppler domain. However, this process is considerably more involved and will not be described in here. The width of the mainlobe contribution in both the range and Doppler domain will also be reduced if not all of the antenna's mainlobe illuminates the ground. However, this effect will not be quantified here.

In contrast to the mainlobe contribution, the clutter return from the sidelobes of the antenna forms a broad region in the range-Doppler plane. If the aircraft is flying straight and level and the antenna is isotropic, the range of Doppler shifts present in the sidelobe returns would be symmetric about zero Hertz. In this case the maximum and minimum Doppler shifts occur at the radar horizon in the forward and rear directions respectively. The maxima and minima as a function of range are given by substituting Equation C.3 into the x-component of Equation A.1 (with the yaw of the aircraft set to zero, i.e. $\xi_p = 0$) and solving for Doppler shift yielding

$$v_{\max}(R) = \frac{2v}{\lambda} \left(\frac{x \cos \zeta_p + z \sin \zeta_p}{R} \right) \quad (2.16)$$

$$v_{\min}(R) = \frac{2v}{\lambda} \left(\frac{-x \cos \zeta_p + z \sin \zeta_p}{R} \right), \quad (2.17)$$

$$\text{where } x = \sqrt{R^2 - z^2} \quad (2.18)$$

$$\text{and } z = R \cos \gamma = \frac{R^2 + h^2 + 2R_E h}{2(R_E + h)}. \quad (2.19)$$

We can use Equation 2.18 for x because the maximum (minimum) Doppler shift in sidelobe clutter at a given range results from ground returns directly in front (behind) the aircraft and hence $y = 0$. The symmetric nature of the sidelobe returns for an aircraft flying straight and level can be seen by substituting a zero aircraft pitch angle ($\zeta_p = 0$) into Equations 2.16 and 2.17.

The asymmetry in the sidelobe returns observed in Figure 2.5, despite the aircraft flying straight and level, is due to the antenna pattern not being modelled in the rear hemisphere. Hence not all of the Earth below the radar is illuminated by the antenna sidelobes. However the asymmetry observed in Figure 2.6 is entirely due to the aircraft diving in this example. In each case the ripple structure in the sum pattern observed in Figure 2.2 is clearly seen. For ranges satisfying $h \leq R \leq h/\sin(\pi/2 - \varphi_0)$ the sidelobe return is dominated by specular reflection from the Earth directly beneath the aircraft. Here φ_0 is angular width of the specular component of the RCS model described in Section 2.1.2. It is the specular reflection from the Earth along with the short range of these returns which gives rise to what is commonly known as the altitude line.

3. The Clutter Signal in the Radar Receiver

How does one calculate the clutter signal in the radar receiver? The first ingredient, a statistical model of the clutter signal, has already been specified in Section 2. The other ingredient which is required is the impulse response of the radar receiver as a function of range and Doppler shift. Ambiguity function analysis will be used here to describe the impulse response of the receiver and Appendix D contains derivations and examples of the ambiguity functions used in this report.

The statistical nature of the clutter signal means that the signal seen in the radar receiver will also be statistical in nature. Hence we need to be able to sample a realisation of the clutter signal in the receiver. There are two approaches one can adopt to do this, *either* sample a realisation of the clutter signal and then fold in the response of the radar receiver *or* sample a realisation of the clutter signal in the receiver directly. The second approach relies on being able to derive a statistical

model of the signal in the receiver where the response of the radar has already been folded in. The first approach is adopted in this report and an algorithm for sampling the clutter signal is presented in this section along with examples of realisations of the clutter signal in the receiver.

3.1 Response of the Radar Receiver in a Ground Clutter Environment

Consider a radar which transmits a signal $s(t)$ and receives a signal $r(t)$ (measured at RF prior to amplification or processing). The signals can be expressed in the complex form as $\psi_s(t) = s(t) + iH[s(t)]$ and $\psi_r(t) = r(t) + iH[r(t)]$ (see e.g. Gabor 1946 and Woodward 1980), where $H[\]$ represents the application of the Hilbert transform. Consider the signal from ground returns at a time t . The return will consist of contributions from patches of ground which were illuminated by signals transmitted a time $\tau = 2R/c$ earlier, where c is the speed of light and we have neglected the effect of range ambiguities for the time being. The contribution to the clutter signal in the receiver from a patch with a Doppler shift, v , will be $\psi_s(t - \tau)e^{2\pi i v t} dZ(\tau, v)$. Here we have expressed the increments of the random clutter field in terms of the two way delay to keep the notation as simple as possible. The total signal received at time t is therefore given by integrating over these contributions yielding

$$\psi_r(t) = \int \psi_s(t - \tau) e^{2\pi i v t} dZ(\tau, v). \quad (3.1)$$

The response of the radar receiver to this signal can be given by calculating the cross ambiguity function of the received signal and a reference signal. If the radar receiver has a matched filter then the reference signal is the transmitted signal and the response of the receiver to the clutter signal is found by substituting Equation 3.1 into Equation D.1 giving

$$\chi_{rs}(\tau', v') = \int e^{-2\pi i (v' - v)\tau} \chi_{ss}(\tau' - \tau, v' - v) dZ(\tau, v) = \int \chi_{ss}(\tau' - \tau, v' - v) dZ(\tau, v). \quad (3.2)$$

Here $\chi_{ss}(\tau, v)$ is the ambiguity function of the transmitted signal given by Equation D.2. To simplify Equation 3.2 we have used the result that a random phasor multiplied by a phasor of unit magnitude yields a random phasor with the same magnitude as the original. From Equation 3.2 we can see that the clutter signal in the receiver is given by the two dimensional convolution of the ambiguity function of the transmitted signal with the random clutter field. While the random clutter field is completely uncorrelated in range and Doppler shift (see Section 2) the signal in the receiver is not uncorrelated because of the effect of the receiver processing. This can be seen by calculating the covariance of the clutter signal in the receiver

$$\begin{aligned} \langle \chi_{rs}(\tau'_1, v'_1) \overline{\chi_{rs}(\tau'_2, v'_2)} \rangle &= \iint \chi_{ss}(\tau'_1 - \tau_1, v'_1 - v_1) \overline{\chi_{ss}(\tau'_2 - \tau_2, v'_2 - v_2)} \langle dZ(\tau_1, v_1) \overline{dZ(\tau_2, v_2)} \rangle \\ &= \int \chi_{ss}(\tau'_1 - \tau, v'_1 - v) \overline{\chi_{ss}(\tau'_2 - \tau, v'_2 - v)} d\tau dv \end{aligned} \quad (3.3)$$

where we have used Equation 2.1 for the covariance of the random field. From Equation 3.3 we can see that the signal in the receiver will in general be correlated in both range and Doppler shift, and that the scale on which the signal is correlated will be determined by the ambiguity function of the transmitted signal. The mean clutter power in the receiver is given by setting $\tau' = \tau'_1 = \tau'_2$ and $\nu' = \nu'_1 = \nu'_2$ in Equation 3.3 yielding

$$\left\langle \left| \chi_{rs}(\tau', \nu') \right|^2 \right\rangle = \int \left| \chi_{ss}(\tau' - \tau, \nu' - \nu) \right|^2 d\alpha(\tau, \nu). \quad (3.4)$$

Hence we can see that the mean clutter power in the receiver is given by a two dimensional convolution of the magnitude of the ambiguity function of the transmitted signal squared and the mean clutter power.

While we have only considered a receiver with a matched filter in the above discussion, similar equations may readily be derived for receivers utilising Dolph-Chebyshev weighted and/or 13 bit Barker coded waveforms. See Appendix D for derivations of the response functions for radar receivers utilising either simple pulse trains or 13 bit Barker coded pulse trains as well as Dolph-Chebyshev weighting. In practice the ideal matched filter is often approximated by a low pass filter. Hence the response of a receiver utilising a low pass filter is also derived in Appendix D. In the following discussion we shall continue to consider only the receiver utilising a matched filter although examples of the clutter signal will also be given for other types of receivers.

3.2 Sampling the Clutter Signal in the Receiver

There are two approaches to sampling a realisation of the clutter signal in the receiver. Either we can sample a realisation of the random clutter field which we then convolve with the ambiguity function of the transmitted signal (using Equation 3.2) or we can calculate the covariance of the signal (using Equation 3.3) and use this to generate a realisation of the clutter signal in the receiver directly.

Let us consider the first approach and examine Equation 3.2 in more detail. Consider a radar transmitting a waveform consisting of a pulse train with pulse repetition interval T_r . For such a waveform only ranges less than one pulse repetition interval (PRI) are unambiguous. Similarly only Doppler shifts less than the pulse repetition frequency, $1/T_r$, are unambiguous. The result is that the clutter returns from all of the ambiguous ranges and Doppler shifts are folded onto the unambiguous range-Doppler interval and the receiver actually sees the superposition of all of these contributions. Here the effect of the range and Doppler ambiguities are taken into account by the impulse response of the radar. In Appendix D the impulse response of a simple pulse train is derived and by examining Equations D.1 and D.4 we can see that the response of the receiver consists of a grid of "spikes" separated by the PRI in the range domain and the PRF in the Doppler domain. If the radar response is

uniform in each of the ambiguous range-Doppler intervals, i.e. in the region between the "spikes", then we can make the approximation

$$\chi_{rs}(\tau', \nu') \approx \sum_m \sum_n \int_{\tau_u} \int_{\nu_u} \chi_{ss}(\tau' - \tau, \nu' - \nu) dZ(\tau + m\tau_u, \nu + n\nu_u), \quad (3.5)$$

where the integrals are now over a single unambiguous delay $\tau_u = T$, and Doppler shift $\nu_u = 1/T_r$. Recall that the clutter signal is modelled as a zero mean, complex Gaussian random process and so it is not necessary to sample a realisation of the entire random field and sum contributions from each of the ambiguous range-Doppler interval individually. Rather, one can fold the clutter power from the entire random field into the unambiguous range-Doppler interval and sample a realisation of the effective field in that interval alone. Hence, Equation 3.5 can be re-written as

$$\chi_{rs}(\tau', \nu') \approx \int_{\tau_u} \int_{\nu_u} \chi_{ss}(\tau' - \tau, \nu' - \nu) dZ_{\Sigma}(\tau, \nu), \quad (3.6)$$

where $Z_{\Sigma}(\tau, \nu)$ is a random process with uncorrelated increments whose covariance is given by

$$\langle dZ_{\Sigma}(\tau_1, \nu_1) \overline{dZ_{\Sigma}(\tau_2, \nu_2)} \rangle = \sum_m \sum_n d(\tau_1 + m\tau_u, \nu_1 + n\nu_u) \delta(\tau_1 - \tau_2) \delta(\nu_1 - \nu_2). \quad (3.7)$$

The sampling algorithm has thus been reduced from sampling the clutter field and performing a two dimensional convolution over the entire range-Doppler domain, to sampling an effective field on the unambiguous range-Doppler interval and performing a two dimensional convolution over a single interval.

The second method of sampling a realisation of the signal in the receiver relies on being able to colour a zero mean complex white noise process so that the resulting random process has the desired covariance. Consider a random sequence $X = \{X_n\}$, with covariance matrix $C = \langle X \overline{X}^T \rangle = TT^T$, where T is a lower triangular matrix and the superscript T signifies the transpose of the matrix. A realisation of the random process can be generated by the equation $X = TW$, where W is a vector containing samples of zero mean complex white noise process with unit spectral density. Here, T can be thought of as the matrix required to colour the white noise process, W , so that the resulting sequence has the required covariance. To demonstrate the utility of this technique consider the response of the radar receiver to white noise. Let the receiver signal be $\psi_r(t) = n(t)$, where $n(t)$ is a zero mean, complex random process with covariance $\langle n(t) \overline{n(s)} \rangle = N_o \delta(t - s)$, and N_o is the spectral density of the noise. The noise signal in a matched receiver is (using Equation D.1)

$$\chi_{rs}(\tau, \nu) = \int_{-\infty}^{\infty} n(t) \overline{\psi_s(t - \tau)} e^{-2\pi i \nu t} dt \quad (3.8)$$

and the covariance of the signal is given by

$$C = \left\langle \chi_{rs}(\tau_1, v_1) \overline{\chi_{rs}(\tau_2, v_2)} \right\rangle = N_o e^{-2\pi i (v_1 - v_2) \tau_2} \chi_{ss}(\tau_1 - \tau_2, v_1 - v_2), \quad (3.9)$$

which is stationary except for the phase term. Hence, to sample a realisation of the noise in the receiver one needs only to decompose C to find the matrix T , sample a vector W , and then perform a matrix multiplication. This approach is particularly beneficial when the covariance matrix is stationary since then the covariance matrix calculation and decomposition only needs to be performed once. The benefits of this approach are largely nullified in the case of sampling the clutter signal in the receiver since the covariance of the signal (Equation 3.3) is not stationary and also does not reduce to a simple form as in the case for the white noise example above.

3.3 Implementation Issues

From the discussion in Section 3.2 we can see that to implement the chosen sampling method we are required to evaluate a two dimensional Fourier transform (Equation 3.3). Rather than evaluating the convolution directly, we will take the Fourier transforms of the ambiguity function and the sampled random field, multiply the transforms element-by-element and then take the inverse Fourier transform to give the signal in the receiver. The Fourier transforms are implemented using a two dimensional fast Fourier transform (FFT) (see e.g. Press *et al* 1987).

To implement the 2D FFTs numerically we need to calculate the ambiguity function and sample the clutter field on a grid of points. How finely do we need to sample the grid points? Ultimately we are interested in calculating the signal "seen" by the radar receiver which typically measures the signal in a grid of range-Doppler bins. Hence, we need only sample at half the spacing of the range-Doppler bins to preserve all the information in the signal seen by the receiver. However some care needs to be exercised in implementing the clutter sampling algorithm because if we sample the clutter field too finely its increments will no longer be uncorrelated. This in turn would invalidate the statistical model of the clutter signal described in Section 2.

From Appendix D we can see that the two dimensional Fourier transform of the ambiguity function is the Rihaczek distribution (Equation D.28) which may be evaluated analytically. Hence we only need to evaluate the two dimensional Fourier transforms of the sampled clutter field and the result of the element-by-element multiplication numerically. This procedure potentially saves some computation time, however for the present analysis we have calculated the Fourier transform of the ambiguity function numerically. We envisage implementing the analytical calculation of the Rihaczek distribution at a later date.

3.4 Examples of the Clutter Signal seen by the Radar Receiver

Consider the clutter return shown in Figure 2.5. The mean clutter signal which results when the returns from all of the ambiguous range-Doppler intervals have been folded onto the unambiguous interval is shown in Figure 3.1. Here we have used a PRI of $\tau_u = 64 \mu\text{s}$ (unambiguous range of 9600 m) which corresponds to a PRF of $\nu_u = 15.625 \text{ kHz}$. The mainlobe contribution can again be clearly seen centred about 10 kHz. However the fine detail in the sidelobe return has now been smeared out due to the folding. From Figure 3.1 we can also see that there is a sharp ridge in the clutter return at a range of about 5000 m which is produced by returns from directly beneath the aircraft. The ridge comes about because there are no sidelobe returns from ranges less than the altitude of the aircraft. Hence the power seen at ranges less than the aircraft's altitude is from subsequent ambiguous range intervals which have much less power than the returns from the altitude line. Here we have also included the effect of transmission blanking by setting the signal in the first range bin to zero. In practice the blanking pulse is usually slightly longer than the pulse duration and hence we are considering the optimal case here. To emphasize the statistical nature of the clutter field we have shown a realisation of the clutter signal in Figure 3.2.

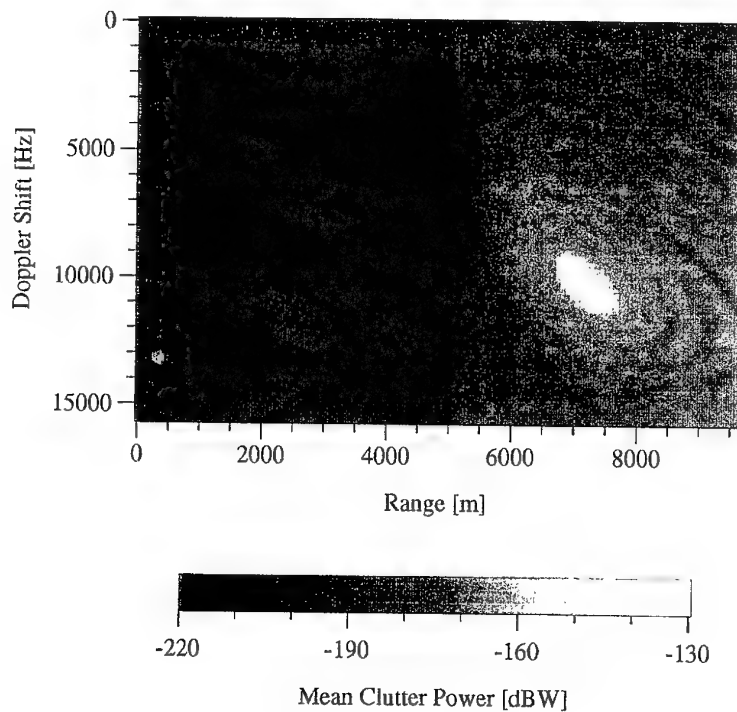


Figure 3.1 The folded mean clutter power corresponding to mean clutter power shown in Figure 2.5. Aircraft parameters are as for Figure 2.5 and we have used a PRF of 15.625 kHz.

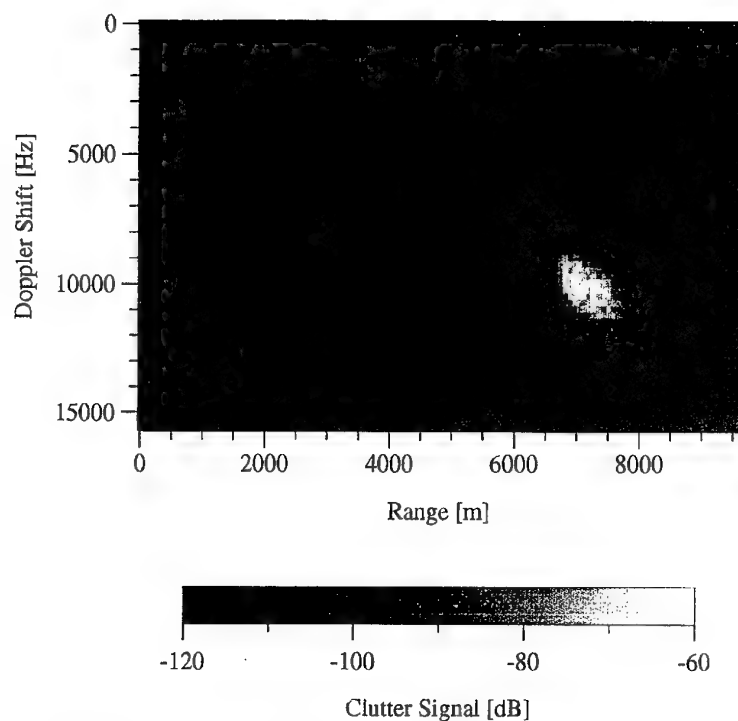


Figure 3.2 A realisation of the folded clutter signal which has the mean clutter power shown in Figure 3.1.

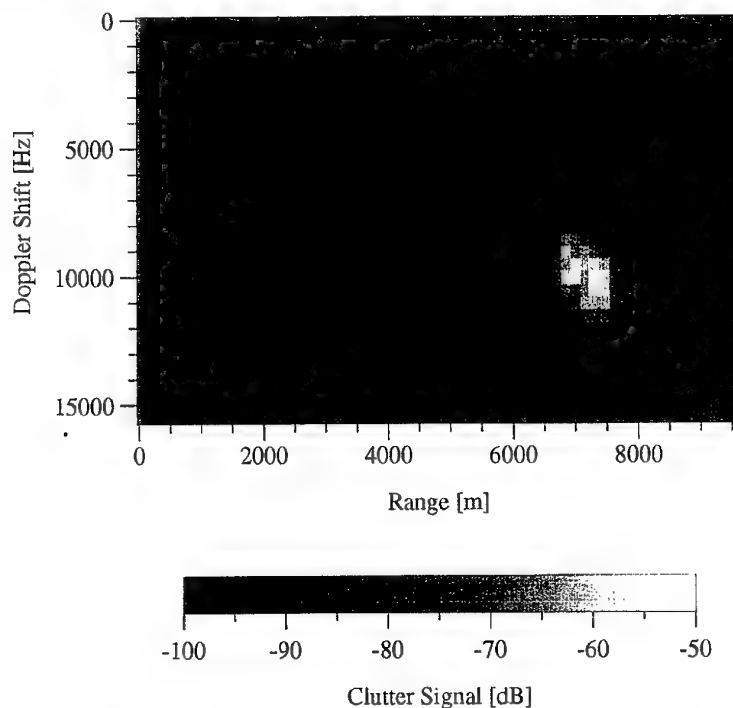


Figure 3.3 An example of the clutter signal seen in a radar receiver utilising a simple pulse train with a Dolph-Chebyshev weighted matched filter. Here we have used 64 range bins, of length $1 \mu\text{s}$ or 150 m, along with 32 Doppler filters.

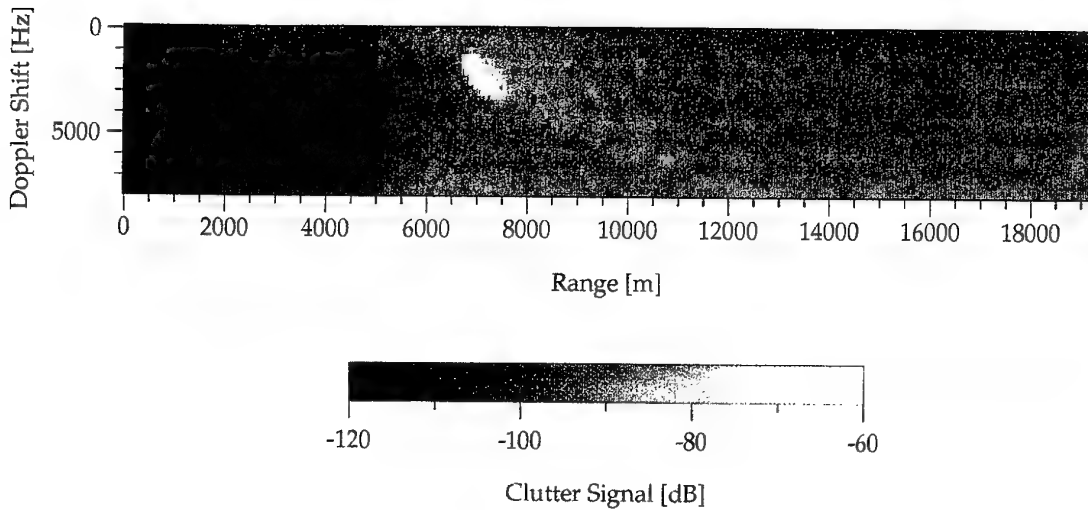


Figure 3.4 Another realisation of the folded clutter signal with mean clutter power shown in Figure 2.5. Here we have used PRI of $128 \mu\text{s}$, which corresponds to an unambiguous range of 19,200 m, and a PRF of 7.8125 kHz. Notice that the transmission blanking require for a 13 bit Barker coded waveform is considerably longer than for the simple pulse train and occupies nearly 2000 m of the unambiguous range interval. The range and Doppler scales have the same relative proportions as used in Figure 3.2 to emphasize the change in the shape of the unambiguous range-Doppler interval with PRF.

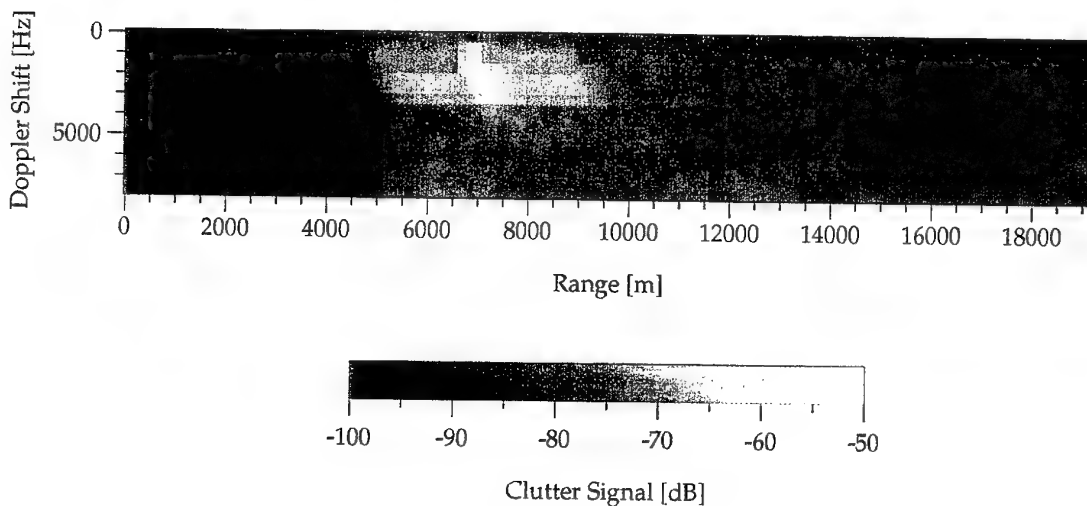


Figure 3.5 An example of the clutter signal seen by a radar receiver utilising a thirteen bit Barker coded pulse train with a Dolph-Chebyshev weighted low pass filter. Here we have used 128 range bins, of length $1 \mu\text{s}$ or 150 m, along with 32 Doppler filters.

The resulting clutter signal in the receiver of a radar using a simple pulse train and a Dolph-Chebyshev weighted matched filter can be calculated by substituting Equation D.11 into Equation 3.6 and is shown in Figure 3.3. In this case we have used 64 range bins, each of which is $1\ \mu\text{s}$ or 150 m long, and 32 Doppler filters. The pixels which make up the range-Doppler image can be clearly seen and now even less of the fine detail in the image remains. From Figure 3.3 we can also see that mainlobe clutter and the altitude line are the dominant features in the signal "seen" by the receiver. Clearly both of these features can significantly increase the clutter background with which a target has to compete and so affect the performance of the radar. Measures to reduce the impact of mainlobe clutter and the altitude line are discussed in Section 4.

If a 13 bit Barker coded waveform is used then the transmission blanking pulse must be significantly longer, as can be seen from Figure 3.4 where we have shown a second realisation of the folded clutter signal. In this case we have used a PRI of $128\ \mu\text{s}$, which corresponds to an unambiguous range of 19,200 m, and a PRF of 7.8125 kHz. We have used the range and Doppler scales in Figure 3.4 have the same relative scales as used in Figure 3.3 to emphasize the way in which the shape of the unambiguous range-Doppler interval changes with PRF. Notice also that the position of the mainlobe has changed relative to the unambiguous Doppler interval. The resulting clutter signal in the receiver of a radar using a Barker coded waveform and a Dolph-Chebyshev weighted low pass filter (calculated by substituting Equation D.25 into Equation 3.6) is shown in Figure 3.5. We can see that the mainlobe has now been significantly smeared due to the range sidelobes in the response of the radar. Much of the fine detail in the image has again been smeared out due to the signal processing in the receiver.

4. Target Detection and Tracking in Ground Clutter

The ability to track manoeuvring targets is an important function of APDRs. Target tracking enables good estimates and predictions of the target's position to be made. Kalman filtering is often used to implement target tracking. This is because the Kalman filter is the optimal estimator for stochastic linear dynamic systems. While the dynamical equations for target tracking by an APDR are in fact non-linear, they can be linearised so that they are in a form suitable for Kalman filtering. The Kalman filter approach also provides predictions of state variables as a natural part of the formalism. The application of Kalman filtering to APDRs has been discussed extensively in the literature. See Singer (1969), Pearson (1971) and Pearson and Stear (1972) for some of the earliest discussions on applying Kalman Filtering to target tracking by APDRs.

A high fidelity model of an APDRs has been developed within EWD. The model includes accurate representations of the antenna gain, radar response, automatic gain control (AGC), Kalman filters and the servomechanism used to drive the antenna.

The model has been kept as generic as possible and so can be thought to represent a class of APDRs. The model does not include any representation of ground clutter and a natural development of the model is to include a high fidelity representation of ground returns.

In Section 3 we saw that mainlobe clutter and altitude line were the dominant clutter features "seen" by the receiver. If a target should be obscured by either of these features then clearly the radar receiver will have difficulty detecting the target due to the increased background signal. We also saw in Section 3 that the position of both clutter features on the unambiguous range-Doppler interval are dependent on the PRF because of the ambiguous nature of the waveform used in MPRF modes. The position of a target on the unambiguous range-Doppler interval is similarly determined by the PRF. Therefore, it is possible to minimise the impact of mainlobe clutter and altitude line on target detection and tracking by selecting the PRF so that the target only has to compete against sidelobe clutter. Hence we can see that the inclusion of clutter is crucial to any computer model of an APDR since minimisation of the impact of clutter is a major design constraint on the signal processing used.

To model the PRF selection algorithms used by the APDR, not only do we need knowledge of the position of the dominant clutter features but also a knowledge of which of the range-Doppler bins are used for target detection and so must be kept clear of corruption. Hence we will give a brief overview of target detection in APDRs before discussing PRF selection in detail. The inclusion of clutter in the computer model required some major modifications to the code and these are described before the section is concluded with examples of target tracks with and without clutter included.

4.1 Target Detection

Target detection by an APDR is typically achieved by some form of constant false alarm rate (CFAR) processing. CFAR detection is implemented by making an estimate of the background in the range-Doppler bins containing the target and then setting a detection threshold to achieve a desired false alarm rate. In doing this we must make assumptions about the distribution of the back-ground signal, e.g. that the amplitude is Rayleigh distributed. The background in the target bins may consist of thermal noise, ground clutter, quantisation noise and anything else which is not the "target". One method of estimating the contribution these unwanted signals make to the target bins is to average the background over regions of the range-Doppler plane. These "CFAR processing regions" need to be as close to the target bins as possible, without undue contamination by the target, so that the estimated background is representative of the signal in the target bins. In practice, this can be achieved in any number of ways. For example, a ring of bins around the target, as shown in Figure 4.1, could be used for CFAR processing. In this case notice that the

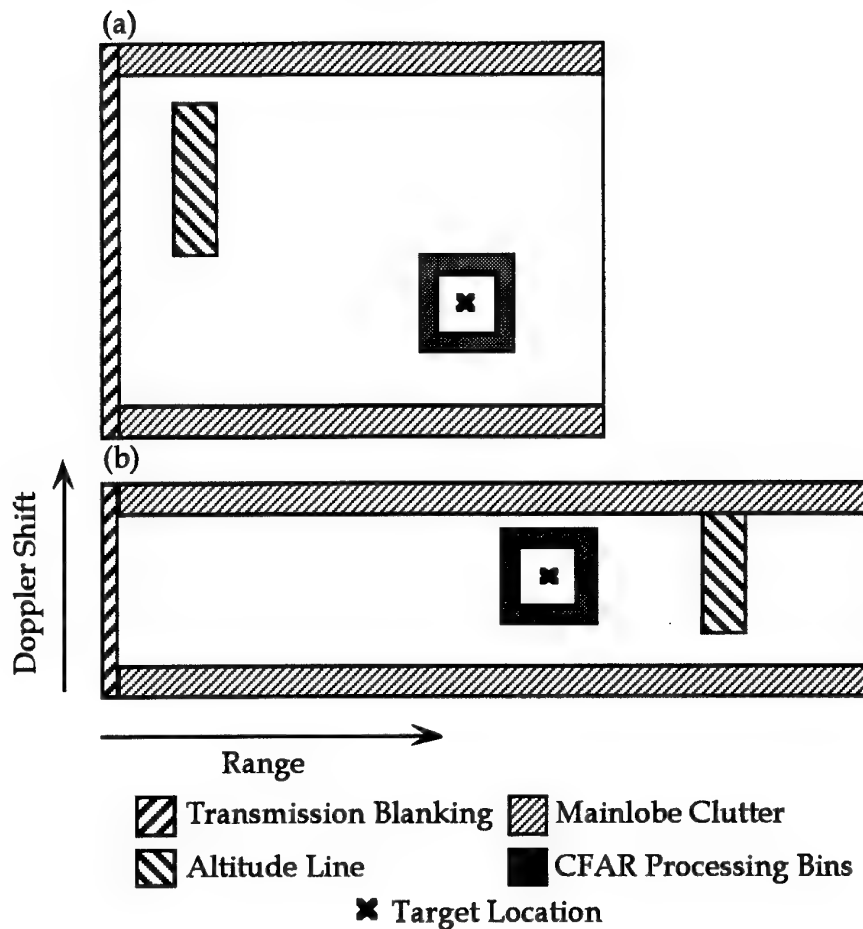


Figure 4.1 A schematic diagram showing the main features on the unambiguous range-Doppler interval. Here we have notionally shown two of the medium PRFs, (a) and (b), to demonstrate how the dimensions of the unambiguous range-Doppler interval and the position of the target and clutter can change with PRF. A hypothetical example of the range-Doppler bins which could be used for CFAR processing are also shown.

estimate of the background will be corrupted by the target since both range and Doppler sidelobes extend into the CFAR processing region if Barker coding is used.

The CFAR processing scheme described above is also known as cell averaged CFAR or CACFAR. Other variants are greatest of CFAR (GOCFAR) processing and smallest of CFAR (SOCFAR) processing in which the range-Doppler bin with the greatest or the least power in the CFAR region is used to estimate the noise in the target bins. GOCFAR is used to bias the detection scheme against clutter edges and

jamming. However this is at the cost of degrading the detection performance when a second target falls within the CFAR processing region. SOCFAR detection schemes have much better performance when a second target falls within the CFAR processing region, however they have poor performance in environments with clutter edges or jamming. Hence in this report we will only consider CACFAR since we will assume that the PRF will have been selected so as to avoid corruption by clutter edges and that the environment is free from jamming. We will also assume that we do not have a second target within the CFAR processing region. See Morris (1988), Levanon (1988) and Nitzberg (1992) for more detailed discussions on CFAR detection.

4.2 PRF Selection

As mentioned earlier, for the effect of clutter on the radar to be minimised, the target bins and the CFAR processing bins must be uncorrupted by mainlobe clutter or the altitude line. This is generally done by selecting the PRF so that the processing swath (the target bins plus CFAR processing bins) is clear of these features. If the radar is operating at a given PRF then we can test to see if the processing swath is uncorrupted by checking that the target position satisfies a set of clearance criteria. Clearance of transmission blanking and altitude line are tested using criteria defined in the range domain since the features are typically only several hundred metres wide in range but several kilohertz wide in Doppler shift. Mainlobe clutter, particularly at long range, is typically only a few hundred hertz wide in Doppler shift but may cover several kilometres in range. Hence clearance of mainlobe clutter is tested in the Doppler domain. If the clearance criteria are not satisfied then the radar must choose a new PRF at which to operate in which the processing swath is not corrupted. Generally there will be several bands of PRFs which satisfy the clearance criteria in the range domain as well as several other bands of PRFs which satisfy the clearance criteria in the Doppler domain. The PRFs where these two sets of bands intersect will satisfy all the clearance criteria. Once these PRFs have been identified the new PRF can be chosen from amongst them. In the discussion which follows we first identify the clearance criteria and then derive the bands of PRFs which satisfy these criteria.

4.2.1 Transmission Blanking and Altitude Line Clearance

Let the clearance criteria for transmission blanking be k_0 range bins before the target and k_1 bins after the target. This means that so long as the transmission blanking pulse is at least k_0 range bins before the target or at least k_1 range bins after the target the CFAR bins around the target will not be corrupted. Similarly let the clearance criteria for the altitude line be l_0 and l_1 range bins, respectively. For the moment we will only consider the case where the altitude line is always in the first unambiguous pulse repetition interval (PRI), i.e. the aircraft's altitude satisfies the inequality

$$(k_0 + l_0)\Delta R < h < R_u^{\min} - (k_1 + l_1)\Delta R \quad (4.1)$$

where $R_u^{\min} = N_{rb}^{\min} \Delta R$ is the minimum unambiguous range, ΔR is the size of the range bins and N_{rb}^{\min} is the minimum number of range bins used in the APDR. If Equation 4.1 is satisfied, the target and CFAR processing bins will be uncorrupted by transmission blanking or altitude line so long as the range of the target satisfies the inequalities

$$k_o \leq \text{int}\left(\frac{R - kR_u}{\Delta R}\right) \leq \text{int}\left(\frac{h}{\Delta R}\right) - l_o \quad (4.2)$$

$$\text{and } \text{int}\left(\frac{h}{\Delta R}\right) + l_1 \leq \text{int}\left(\frac{R - kR_u}{\Delta R}\right) \leq N_{rb} - k_1. \quad (4.3)$$

Here $k = \text{int}(R/R_u)$ is an integer which indicates which of the ambiguous PRIs the target is in, $R_u = N_{rb} \Delta R$ is the unambiguous range and N_{rb} is the number of range bins formed for the present value of the PRF. In both Equations 4.2 and 4.3 the quantity between the inequality signs is simply the range bin number which contains the target.

If the target range does not satisfy Equations 4.2 and 4.3 then we need to calculate the bands of PRFs which do satisfy the range clearance criteria in anticipation of selecting a new PRF. If the target range is less than the unambiguous range, i.e. $R < R_u^{\min} + k_o \Delta R$, then the relationship in the range domain between the target, transmission blanking and altitude line cannot be changed by changing the PRF. In this case the clearance criteria in the range domain are relaxed and only the clearance criteria in the Doppler domain are used to select the new PRF. For ranges which satisfy $R_u^{\min} + k_o \Delta R \leq R \leq R_u^{\max} - k_1 \Delta R$, the bands of PRIs (and hence PRFs) which satisfy the clearance criteria (Equations 4.2 and 4.3) are given by

$$\text{int}\left(\frac{R}{\Delta R}\right) + k_1 \leq N_{rb} \leq N_{rb}^{\max} \quad (4.4)$$

for $k = 0$ and

$$\max\left\{N_{rb}^{\min}, \left(\text{int}\left(\frac{R}{\Delta R}\right) - \text{int}\left(\frac{h}{\Delta R}\right) + l_o\right) / k\right\} \leq N_{rb} \leq \left(\text{int}\left(\frac{R}{\Delta R}\right) - k_o\right) / k \quad (4.5)$$

$$\max\left\{N_{rb}^{\min}, \left(\text{int}\left(\frac{R}{\Delta R}\right) + k_1\right) / (k+1)\right\} \leq N_{rb} \leq \left(\text{int}\left(\frac{R}{\Delta R}\right) - \text{int}\left(\frac{h}{\Delta R}\right) - l_1\right) / k \quad (4.6)$$

for $1 \leq k \leq k_{\max}$, where N_{rb}^{\min} and N_{rb}^{\max} are the minimum and maximum number of range bins formed and $k_{\max} = \text{int}((R - k_o \Delta R) / R_u^{\min})$. Here we have expressed the PRI in terms of the number of range bins formed by the receiver. For longer target ranges which satisfy $R \geq R_u^{\max} - k_1 \Delta R$, it is not possible for the target range to be less than the

unambiguous range for any PRF and hence $k_{\min} = \text{int}((R + k_1 \Delta R) / R_u^{\max})$. Equations 4.5 and 4.6 now give the PRI bands which satisfy the clearance criteria in the range domain for $k_{\min} \leq k \leq k_{\max}$.

For example, the bands of PRIs which satisfy the clearance criteria when $k_o = k_1 = l_o = l_1 = 5$ range bins and the aircraft flies at an altitude of $h = 5$ km are shown as the shaded regions in Figure 4.2. For this plot we have used $N_{rb}^{\min} = 64$ and $N_{rb}^{\max} = 256$. The red shaded regions are formed by PRIs which put the target in the region after the altitude line and before the next transmission blanking pulse (see e.g. Figure 4.1a). Similarly, the blue shaded regions are formed by PRIs which put the target in the region before the altitude line (Figure 4.1b).

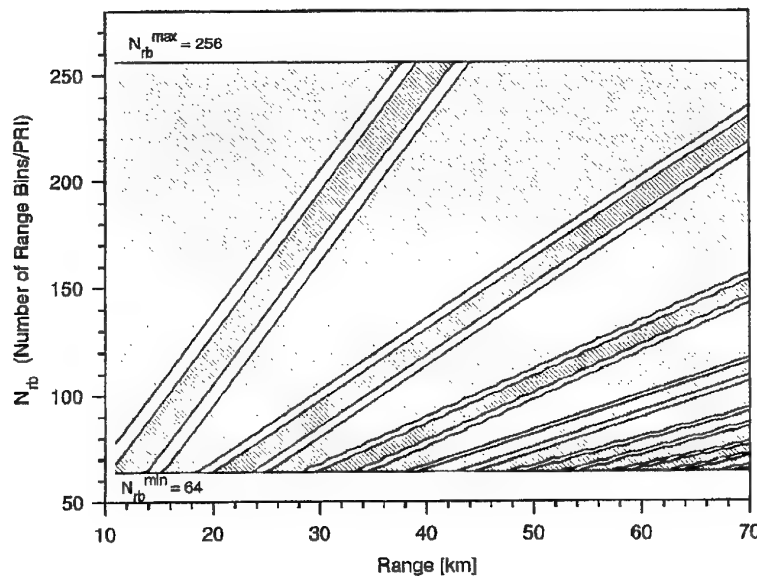


Figure 4.2 A plot of the PRI bands which satisfy the range clearance criteria (Equation 4.1) for an aircraft flying at an altitude of 5000 metres. The red shaded bands are formed by PRIs which put the target after the altitude line and before the next blanking pulse. The blue shaded bands are formed by PRIs which put the target before the altitude line

If the aircraft flies at low altitude so that $h \leq (k_o + l_o) \Delta R$ then the transmission blanking pulse and the altitude line are so close together that it is not possible for the target to be in a range bins between them without corrupting the processing swath. In this case there is only one clearance criterion which is applied in the range domain and is given by Equation 4.2. When this occurs only one band of PRIs, given by Equation 4.4 or 4.6, which satisfies the clearance criterion for each value of k . In

Figure 4.3, we have shown the bands of PRIs which satisfy the clearance criteria for $h = 1$ km. This corresponds to a case where there is no clear region before the altitude line. However, the PRIs which put the target in the clear after the altitude line (the red shaded regions) are now correspondingly larger.

In these examples we have used an arbitrary clearance criterion of five range bins. In practice the clearance criteria are carefully chosen to take into account effects such as the asymmetry of the altitude line in range and the spreading of the altitude line caused by the range sidelobes when using Barker coded waveforms.

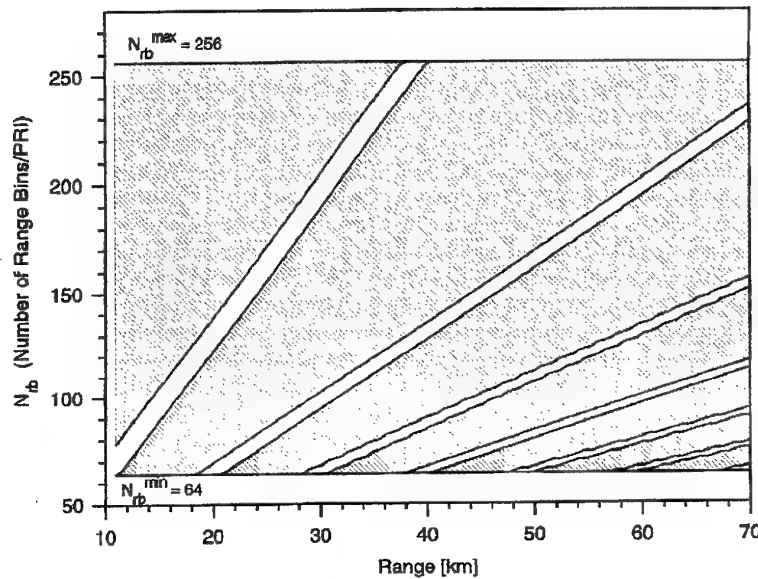


Figure 4.3 A plot of the PRI bands which satisfy the range clearance criteria (Equation 4.1) for an aircraft flying at an altitude of 1000 metres. Bands are defined as for Figure 4.2.

4.2.2 Mainlobe Clearance

In the Doppler domain a frequency offset which corresponds to the frequency of the ambiguous mainlobe clutter immediately below the target is usually introduced during processing. This is done so that the mainlobe clutter is at a Doppler shift of zero Hertz, leaving the central part of the unambiguous Doppler interval free from mainlobe clutter. The offset is given by

$$v_{\text{offset}} = \begin{cases} v_{\text{MLC}} + mv_u, & \text{for } v > v_{\text{MLC}} \\ v_{\text{MLC}} - (m+1)v_u, & \text{for } v < v_{\text{MLC}} \end{cases} \quad (4.7)$$

where v_{MLC} is the unambiguous mainlobe clutter (MLC) frequency and

$$m = \text{int}\left(\left|v - v_{\text{MLC}}\right|/v_u\right). \quad (4.8)$$

The clearance criteria for ensuring that the processing swath is not corrupted by MLC is then given by the inequality

$$v_o \leq (v - v_{\text{offset}}) \leq (v_u - v_o) \quad (4.9)$$

where $v_o = \Delta v_{\text{MLC}} + v_{\text{GMT}}$ is the clearance margin of the target expressed in hertz, Δv_{MLC} is the 3 dB half width of the MLC and v_{GMT} is a threshold included to avoid tracking ground moving targets (GMTs).

For the case where the clearance margin is small enough so that it does not span even the smallest PRF used in MPRF, i.e. $2v_o < v_u^{\min}$, there are clear regions in the Doppler domain for all the available PRFs. The bands of PRIs which satisfy the clearance criteria (Equation 4.9) are then given by

$$\max\left\{N_{rb}^{\min}, \text{int}\left(\frac{m}{(|v - v_{\text{MLC}}| - v_o)T_p}\right)\right\} \leq N_{rb} \leq \min\left\{N_{rb}^{\max}, \text{int}\left(\frac{m+1}{(|v - v_{\text{MLC}}| + v_o)T_p}\right)\right\}. \quad (4.10)$$

$$\text{where } m_{\min} \leq m \leq m_{\max} \quad (4.11)$$

$$\text{with } m_{\min} = \begin{cases} 0, & \text{for } (v_u^{\min} + v_o) \leq |v - v_{\text{MLC}}| \leq (v_u^{\max} - v_o) \\ \text{int}\left((|v - v_{\text{MLC}}| + v_o)/v_u^{\max}\right), & \text{for } |v - v_{\text{MLC}}| > (v_u^{\max} - v_o) \end{cases} \quad (4.12)$$

$$\text{and } m_{\max} = \text{int}\left(\frac{|v - v_{\text{MLC}}| - v_o}{v_u^{\min}}\right). \quad (4.13)$$

Similarly for the case where $v_u^{\min} \leq 2v_o \leq v_u^{\max}$ only PRFs in the range, $2v_o \leq v_u \leq v_u^{\max}$, satisfy the clearance criteria and hence the bands of PRIs are given by

$$\max\left\{N_{rb}^{\min}, \text{int}\left(\frac{m}{(|v - v_{\text{MLC}}| - v_o)T_p}\right)\right\} \leq N_{rb} \leq \min\left\{\text{int}\left(\frac{1}{2v_o T_p}\right), \text{int}\left(\frac{m+1}{(|v - v_{\text{MLC}}| + v_o)T_p}\right)\right\}.$$

$$\text{where the bounds on } m \text{ are again given by Equation 4.11 but now} \quad (4.14)$$

$$m_{\max} = \text{int}\left(\frac{|v - v_{\text{MLC}}| - v_o}{2v_o}\right). \quad (4.15)$$

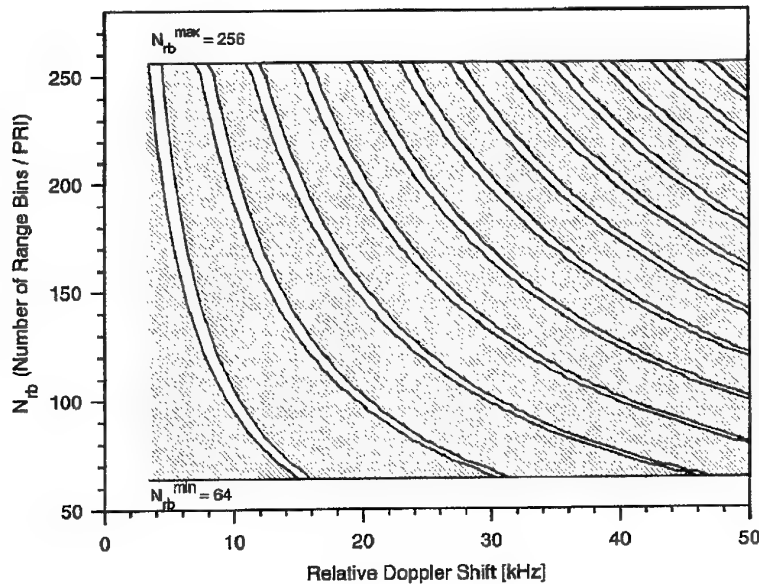


Figure 4.4 A plot of the PRI bands (red shaded regions) which satisfy the Doppler clearance criteria (Equation 4.9) as a function of the relative Doppler shift, i.e. the difference between the target Doppler shift and the mainlobe clutter frequency, for $v_o = 500$ Hz.

For the case where $2v_o > v_u^{\max}$ there are no PRFs which satisfy the clearance criteria (Equation 4.9) and hence the new PRF is selected based only on the clearance criteria in the range domain. Notice also that if the target Doppler shift and the unambiguous mainlobe clutter frequency are too close together, i.e. $|v - v_{MLC}| < v_u^{\min} + v_o$, then the relationship between them cannot be changed by changing the PRF. When this occurs the PRF is again selected based on the clearance criteria in the range domain.

In Figure 4.4 the PRI bands which satisfy the clearance criteria in the Doppler domain when $v_o = 500$ Hz are shown. The PRI bands are again shown by the red shaded regions. Here the Doppler shift of the target relative to the Doppler shift of the mainlobe has been plotted on the horizontal axis. Similarly the PRI bands for $v_o = 2.5$ kHz are shown in Figure 4.5 for comparison. In this case notice that the maximum PRI has reduced because some of the available PRFs are no longer large enough to satisfy the clearance criteria.

4.2.3 Implementation of the PRF selection algorithm

Consider an aircraft flying at 5000 m with a radar on board which is operating with Doppler margin of $v_o = 500$ Hz. In practice, the radar receiver will have some mechanism for measuring the 3 dB half width of mainlobe clutter and so v_o will be

determined dynamically. The bands of PRIs which satisfy the clearance criteria are given by Figure 4.2 and 4.4. Cuts across these figures at the target range and Doppler shift give the PRI bands which satisfy the clearance criteria in the range and Doppler domains. The intersection of these bands then give the PRIs which satisfy all the clearance criteria. How do we choose amongst the PRIs which satisfy all of the criteria? Ideally we would like to choose the new PRF of the radar so as to minimise the number of PRF changes which are required as the target is tracked. One way of achieving this is to calculate which of the PRI bands satisfying all the clearance criteria is the largest and then sampling the new PRF from this band. The selection routine might be as simple as calculating the PRF which corresponds to midpoint of this PRI band. If no intersections between the PRI bands satisfying the range and Doppler clearance criteria exist, then the clearance criteria may be relaxed in a series of stages until a clear region is found. This comes at the cost of corrupting some of the CFAR bins.

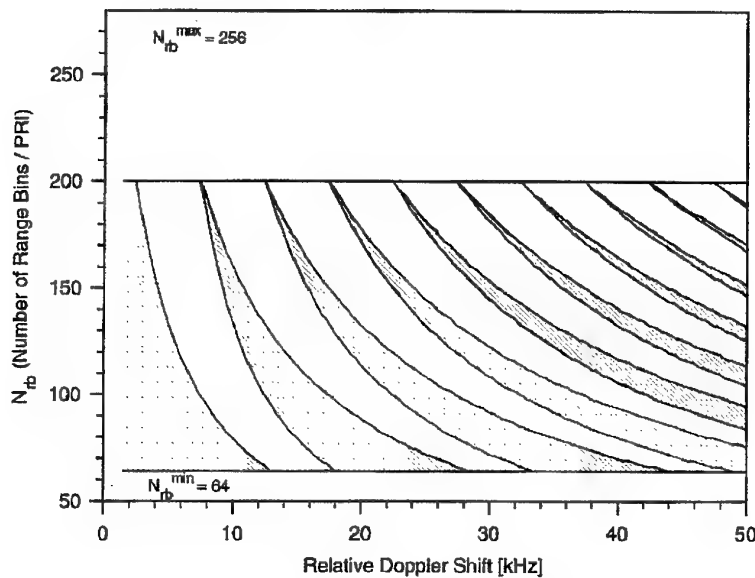


Figure 4.5 A plot of the PRI bands (red shaded regions) which satisfy the Doppler clearance criteria (Equation 4.9) as a function of the relative Doppler shift, i.e. the difference between the target Doppler shift and the mainlobe clutter frequency, for $v_o = 2500$ Hz.

4.3 Automatic Gain Control

APDRs typically use some form of AGC in their receivers to prevent saturation of components or clipping of signals. A constant AGC gain must be used during each coherent integration period and hence the gain is usually set during the pause PRIs between each processing cycle. For the work described in this report, we model the action of the AGC by finding the range-Doppler bin with the maximum average power level and then setting the gain for the next processing cycle so that the probability that the signal in this bin exceeds the dynamic range of the receiver's memory is minimal. Consider a target with delay, τ_T , and Doppler shift, ν_T . The signal in the RF portion of the receiver prior to amplification is given by

$$\psi_r(t) = \int \psi_s(t - \tau) e^{2\pi i \nu \tau} dZ(\tau, \nu) + a_T(t) \psi_s(t - \tau_T) e^{2\pi i \nu_T t} + n(t), \quad (4.16)$$

where $a_T(t)$ and $n(t)$ are random processes which represent the amplitude of the return from the target and thermal noise in the receiver. The average power in the range-Doppler bins of the receiver is therefore given by

$$\langle |\chi_{rs}(\tau', \nu')|^2 \rangle = \int |\chi_{ss}(\tau' - \tau, \nu' - \nu)|^2 dC(\tau, \nu) + A |\chi_{ss}(\tau' - \tau_T, \nu' - \nu_T)|^2 + N_o, \quad (4.17)$$

where $A = \langle |a_T(t)|^2 \rangle$ and $N_o = \langle |n(t)|^2 \rangle$ are the average power of the target and the thermal noise, respectively. Once the maximum average power level has been found, the gain of the receiver is given by

$$g = V / \left(F \sqrt{\max \left\{ \langle |\chi_{rs}(\tau', \nu')|^2 \rangle \right\}} \right), \quad (4.18)$$

where V is the magnitude of the largest number which can be stored in the bulk memory of the radar signal processor and F is a factor which is set by the probability of clipping. This approach is idealised and the gain which results is optimal in the sense that, given F , the gain is maximised.

4.4 Modifications to the Model

The inclusion of ground clutter and PRF selection logic required significant modifications to the existing model of the APDR. The routines which sampled the thermal noise on the range-Doppler plane and place a target on the range-Doppler plane had to be replaced, along with the routine for calculating the gain of the radar. With the inclusion of clutter in the model, a range and Doppler offset had to be calculated before each coherent integration period to correctly place the target and clutter in the processing swath. This process models the action of an ideal variable delay generator and an ideal variable frequency oscillator in the receiver. More

realistic responses for these components will be added at a later stage. Routines for calculating a new PRF and checking to see if the old PRF satisfied the target clearance requirements were also added to the model.

4.5 An Example of Target Tracking in Clutter

An example of some of the output from the APDR model for a target track calculated without including clutter is shown in Figure 4.6. In this example the radar is on board an aircraft flying straight and level with a velocity of 300 ms^{-1} at an altitude of 1000 metres. The target is originally at a range of 20 kilometres and is flying at 300 ms^{-1} towards the aircraft at an altitude of 900 metres. For this particular example, we have set the radar to have no pulse compression and to use a Dolph-Chebyshev weighted matched filter. In Figure 4.6a we have shown the target signal to noise ratio (SNR) for the first five seconds of the track. The SNR is fairly uniform during the track because the target only has to compete with thermal noise and quantisation noise. In Figures 4.6b and 4.6c we have shown the range and Doppler discriminants (solid line) which arise during the track. In each case the discriminants have been calculated using a split gate discriminator. The bounds on the discriminants, calculated by multiplying the variance of the residuals by a factor of 3.889 so that the probability of false alarm is 10^{-4} , are also shown in Figures 4.6b and 4.6c (dotted line). Again these plots are typical of a track in a non-clutter environment.

In Figure 4.7 we have shown the output from the model for the same scenario when clutter is included. Comparing the signal to noise ratios, we can see that the inclusion of clutter has a significant effect. This is because as the target moves on the range-Doppler plane the background is no longer uniform. The effect of the PRF changes is also clearly seen in Figure 4.7a from the steps in the signal to noise ratio. We can also see the PRF changes in Figures 4.7b and 4.7c where they manifest as jumps in the bounds on the residuals. The range and Doppler discriminants are also larger and this indicates that the track is not as good. Despite this, track is maintained in the clutter environment.

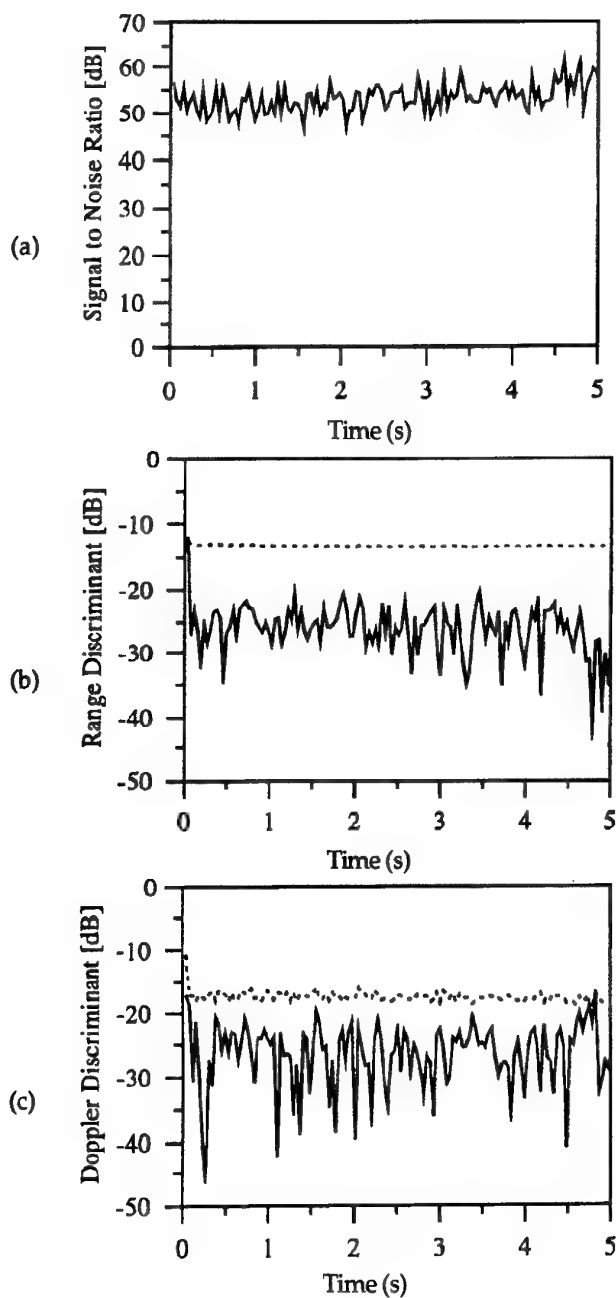


Figure 4.6 A plot of some of the output from the computer model when ground clutter is not included. See text for a description of the scenario. Shown are (a) target signal to noise ratio, and the (b) range and (c) Doppler discriminants (solid line). The bounds on the discriminants (dotted line), based on the range and Doppler residuals, are also shown.

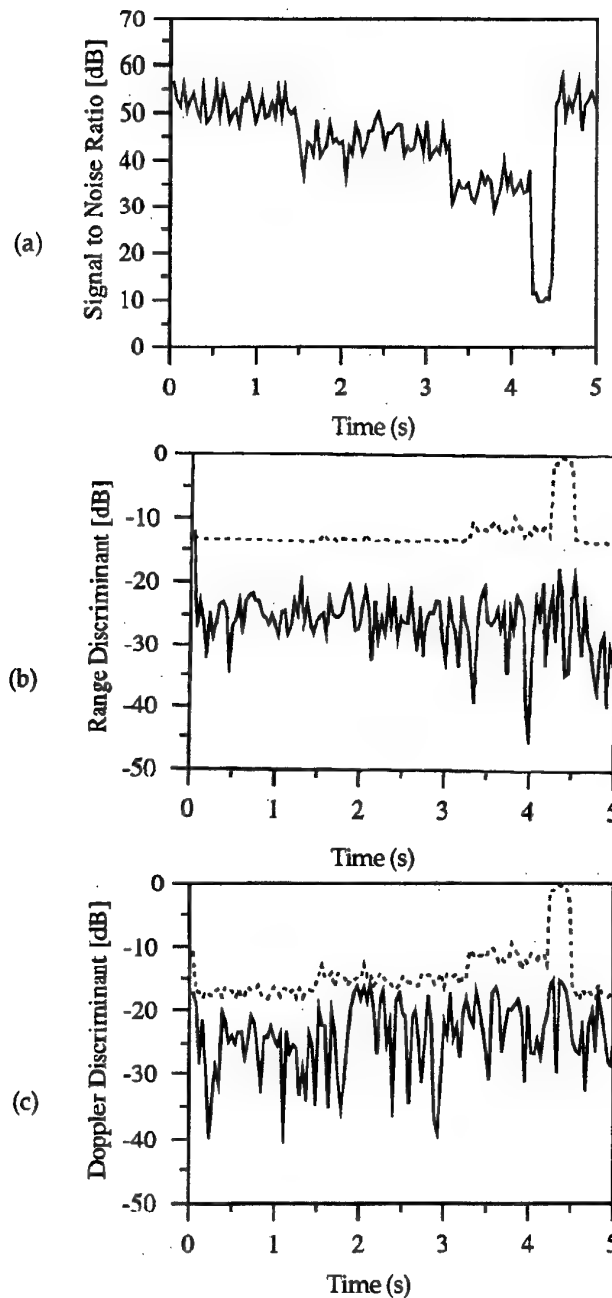


Figure 4.7 A plot of some of the output from the computer model when ground clutter is included. See text for a description of the scenario. Shown are (a) target signal to noise ratio, and the (b) range and (c) Doppler discriminants (solid line). The bounds on the discriminants (dotted line), based on the range and Doppler residuals, are also shown.

5. Conclusions

In this report we presented a model of ground clutter in which the clutter signal is represented by a Gaussian random field with uncorrelated increments. This model was used to sample the clutter signal in the receiver of an airborne pulse Doppler radar. Several types of receivers were considered including those with Dolph-Chebyshev weighted, 13 bit Barker coded waveforms. The clutter calculation presented here differs from other calculations presented in the open literature in a number of ways. For example, no significant approximations have been made in the calculation and the phase information in the clutter signal has been preserved throughout the radar signal processing chain to ensure that the correlations in the receiver are calculated correctly.

The resulting clutter calculation algorithm has been included in the existing computer model of an airborne pulse Doppler radar. Pulse repetition frequency selection routines have also been added to the computer model. From the analysis presented in this report, we can see that clutter has a significant impact on the way in which medium pulse repetition frequency tracking is implemented in airborne pulse-Doppler radars. For example, the need to minimise the effect of mainlobe clutter and altitude line constrains which of the PRFs are available to the radar at any given time. We can conclude from the analysis presented here that it is vital to include the effects of ground clutter to accurately model the performance of the radar.

At present, the computer model runs quite slowly relative to the original version of the code in which no ground clutter was included, however it is hoped that significant improvement in run time can be achieved by optimising some of the routines for the clutter calculation and also by using optimisation when compiling the code. With these improvements, the code will be used to analyse the performance of medium pulse repetition frequency target tracking in a clutter environment.

6. Acknowledgments

I would like to acknowledge the guidance and advice of Dr. T. A. Winchester in this work. This work has been undertaken as part of the task ADA 94/352. I would like to thank Tom Winchester, Peter Gerhardy, Gino Beltrame, and the referee, Richard Hawkes, for providing constructive comments on the manuscript.

7. References

Blahut, E.E., Miller, W., and Wilcox, C.H., 1991 "Radar and Sonar: Part I", Springer-Verlag, New York.

- Boashash, B., 1992, "Time-Frequency Signal Analysis, Methods and Applications", Longman Cheshire, Melbourne.
- Cohen, L., 1989, "Time-Frequency Distributions-A Review", Proceedings of the IEEE, 77, 941-981.
- Farrell, J.L., and Taylor, R.L., 1964, "Doppler Radar Clutter", IEEE Transactions on Aerospace and Navigational Electronics, ANE-11, 162-172.
- Friedlander, A.L., and Greenstein, L.J., 1970, "A Generalized Clutter Computation Procedure for Airborne Pulse Doppler Radars", IEEE Transactions on Aerospace and Electronic Systems, AES-6, 51-61.
- Gabor, D., 1946, "Theory of Information", Part III, IEE, 93, 429-457.
- Harris, F.J., 1978, "On the Use of Windows for Harmonic Analysis with the Discrete Fourier Transform", Proceedings of the IEEE, 66, 51- 83.
- Jao, J.K., and Goggins, W.B., 1985, "Efficient, Closed-Form Computation of Airborne Pulse-Doppler Radar Clutter", in Proceedings of IEEE/IEE International Radar Conference RADAR 85, 17-22.
- Levanon, N., 1988, "Radar Principles", Wiley, New York.
- Mitchell, R.L., 1978, "Radar Signal Simulation", Artech House, Dedham, Massachusetts.
- Morris, G.V., 1988, "Airborne Pulsed Doppler Radar", Artech House, Norwood, Massachusetts.
- Nitzberg, R., 1992, "Adaptive Signal Processing for Radar", Artech House, Boston, Massachusetts.
- Pearson, J.B., 1971, "Basic Studies in Airborne Radar Tracking Systems", Ph. D. Thesis, University of California, Los Angeles.
- Pearson, J.B., and Stear, E.B., 1972, "Kalman Filter Applications in Airborne Radar Tracking", IEEE Transactions on Aerospace and Electronic Systems, AES-10, 319-329.
- Press, W.H., Flannery, B.P., Teukolsky, S.A., and Vetterling, W.T., 1987, "Numerical Recipes, The Art of Scientific Computing", Cambridge University Press, Cambridge.
- Rihaczek, W., 1969, "Principles of High Resolution Radar", McGraw-Hill, New York.

Ringel, M.B., 1977, "An Advanced Computer Calculation for Ground Clutter in an Airborne Pulse Doppler Radar", in *Proceedings of the IEEE 1977 National Aerospace and Electronics Conference*, 921-928.

Sandhu, G.S., 1981, "A Real-Time Clutter Model for an Airborne Pulse Doppler Radar", DRSMI-RDR 102-071, US Army Missile Command, Redstone Arsenal, Alabama.

Singer, R.A., 1969, "Estimating Optimal Tracking Filter Performance for Manned Manoeuvring Targets", *IEEE Transactions on Aerospace and Electronic Systems*, **AES-6**, 473-483.

Woodward, P.M., 1980, "Probability and Information Theory with Application to Radar", Pergamon Press, London.

Appendix A

Transformation Matrices

Consider the reference frames illustrated in Figure 2.1. The platform frame is related to the inertial frame by a rotation through an angle ξ_p (yaw) about the z -axis followed by a rotation through an angle ζ_p (pitch) about the y' -axis, and finally a rotation through angle ς_p (roll) about the x_p -axis. All rotations are in a clockwise direction when looking along the axis of rotation and the primed axes are defined to indicate the intermediate stages of the transformations. The transformation from the inertial frame to the platform frame is therefore given by

$$\bar{r}_p = T_{x_p}(\varsigma_p) T_{y'}(\zeta_p) T_z(\xi_p) \bar{r} \quad (\text{A.1})$$

where $\bar{r} = (x, y, z)$ is a position vector resolved in the inertial frame and $\bar{r}_p = (x_p, y_p, z_p)$ is the same vector resolved in the platform frame. The matrix $T_z(\xi_p)$ is the transformation required to rotate a vector through an angle ξ_p about the z -axis and is given by

$$T_z(\xi_p) = \begin{bmatrix} \cos \xi_p & \sin \xi_p & 0 \\ -\sin \xi_p & \cos \xi_p & 0 \\ 0 & 0 & 1 \end{bmatrix} \quad (\text{A.2})$$

Similarly $T_{y'}(\zeta_p)$ and $T_{x_p}(\varsigma_p)$ are transformation matrices for rotations about the y' and x_p axes, respectively, and are given by

$$T_{y'}(\zeta_p) = \begin{bmatrix} \cos \zeta_p & 0 & -\sin \zeta_p \\ 0 & 1 & 0 \\ \sin \zeta_p & 0 & \cos \zeta_p \end{bmatrix} \quad (\text{A.3})$$

$$T_{x_p}(\varsigma_p) = \begin{bmatrix} 1 & 0 & 0 \\ 0 & \cos \varsigma_p & \sin \varsigma_p \\ 0 & -\sin \varsigma_p & \cos \varsigma_p \end{bmatrix} \quad (\text{A.4})$$

The clutter model described in the body of this report is symmetric relative to the yaw of the aircraft and hence ξ_p has been set to zero to simplify the transformations. This equates to replacing $T_z(\xi_p)$ with the identity matrix in Equation A.1. The transformation from the platform frame to the inertial frame is given by applying the rotations in reverse yielding

$$\vec{r} = T_z(-\xi_p)T_{y'}(-\zeta_p)T_{x_p}(-\varsigma_p)\vec{r}_p. \quad (\text{A.5})$$

Similarly the transformation from the platform frame to the antenna frame is given by

$$\vec{r}_a = T_{y_a}(\zeta_a)T_{z_p}(\xi_a)\vec{r}_p \quad (\text{A.6})$$

where $\vec{r}_a = (x_a, y_a, z_a)$ is the vector \vec{r} resolved in the antenna frame, ξ_a and ζ_a are the antenna's azimuth and elevation. The rotation matrices $T_{z_p}(\xi_a)$ and $T_{y_a}(\zeta_a)$ may be found by analogy with Equations A.2 and A.3. The transformation from the antenna frame to the platform frame is again given by applying the rotations in reverse yielding

$$\vec{r}_p = T_{z_p}(-\xi_a)T_{y_a}(-\zeta_a)\vec{r}_a. \quad (\text{A.7})$$

Appendix B

Derivation of the dA in terms of R and ν

Consider the inertial frame shown in Figure B.1. The incremental area, dA , can be written terms of angles ρ and ψ as

$$dA = R_E^2 d(\cos \rho) d\psi. \quad (\text{B.1})$$

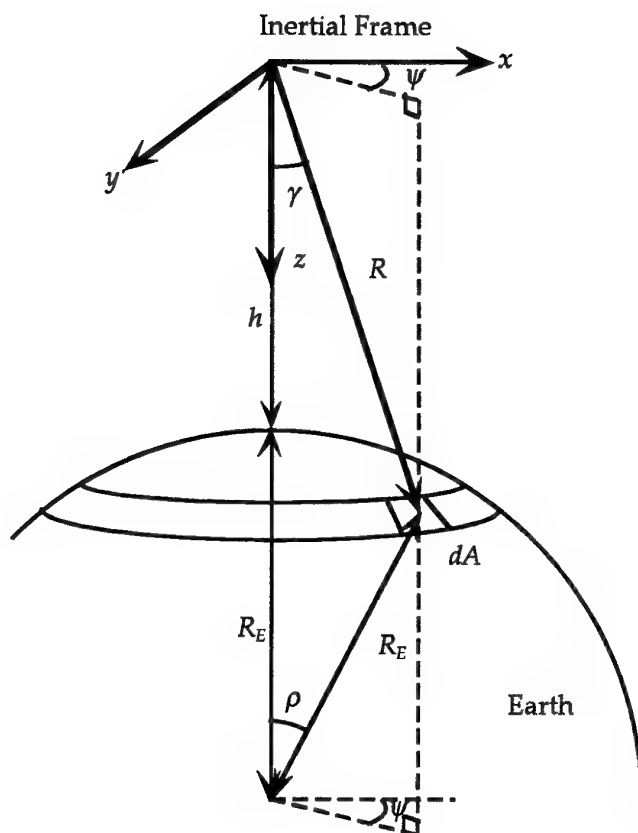


Figure B.1 A schematic diagram of the inertial frame and the Earth.

We can find an expression for $\cos \rho$ by applying the cosine rule and rearranging giving

$$\cos \rho = \frac{R_E^2 + (R_E + h)^2 - R^2}{2R_E(R_E + h)} \quad (\text{B.2})$$

and hence by differentiating and substituting into Equation B.1 we have

$$dA = -\frac{R_E R}{R_E + h} dR d\psi. \quad (\text{B.3})$$

The angles γ and ψ , along with R , form a spherical set of coordinates and so we can express the coordinates of the point at the centre of the incremental area as

$$\vec{r} = \begin{bmatrix} R \sin \gamma \cos \psi \\ R \sin \gamma \sin \psi \\ R \cos \gamma \end{bmatrix}. \quad (\text{B.3})$$

Substituting into the expression for the x -component of the transformation from the inertial frame to the platform frame (Equation A.1 with $\xi_p = 0$) we have

$$x_p = R \sin \gamma \cos \psi \cos \zeta_p - R \cos \gamma \sin \zeta_p. \quad (\text{B.4})$$

Comparison with Equation C.3 yields

$$\cos \alpha = \sin \gamma \cos \psi \cos \zeta_p - \cos \gamma \sin \zeta_p \quad (\text{B.5})$$

which can be differentiated and rearranged to give

$$d(\cos \alpha) = -\sqrt{\cos^2 \zeta_p - \cos^2 \alpha - \cos^2 \gamma - 2 \cos \alpha \cos \gamma \sin \zeta_p} d\psi = -F(R, \psi) d\psi. \quad (\text{B.6})$$

Differentiating Equation 2.5 for the Doppler shift, substituting Equation B.5 and 2.4, and rearranging yields the result

$$dA = \frac{R_E R}{R_E + h} \frac{dR d\nu}{v_{\max} F(R, \psi)}. \quad (\text{B.7})$$

as required.

Appendix C

Mapping (R, ν) to (θ, ϕ)

To evaluate Equation 2.2, we need to be able to solve for the angles θ and ϕ as functions of range and Doppler shift. This equates to solving for the co-ordinates of the point on the Earth's surface define by the vector \vec{r} which has a range, R , and Doppler shift, ν . In general there will be a locus of points on the Earth's surface at a constant range from the radar (called an isorange). The isoranges form circles on the Earth's surface with equation

$$x^2 + y^2 = R^2 - z^2. \quad (C.1)$$

$$\text{Here } z = R \cos \gamma = \frac{R^2 + h^2 + 2R_E h}{2(R_E + h)} \quad (C.2)$$

and is given by inspection of Figure 2.1 and applying the cosine rule. Similarly, all points on a cone of angle α about the direction of the aircraft's velocity, \vec{v} , will have the same Doppler shift. The intersection of this cone with the Earth's surface will form a locus of constant Doppler shift (called an isodop). The isodops form a variety of geometric shapes, depending on range, which can be represented in the platform frame by the equations

$$x_p = R \cos \alpha \quad (C.3)$$

$$\text{and } y_p^2 + z_p^2 = R^2 \sin^2 \alpha. \quad (C.4)$$

Equations C.3 and C.4 can be obtained by projecting the vector \vec{r} onto the x_p -axis and the $y_p z_p$ -plane and then applying the Pythagoras theorem. The coordinates of the point(s) at the intersection of the isorange and the isodop can be found by substituting Equation C.3 into the expression for the x -component of Equation A.1 (ξ_p set to zero as explained in Appendix A) and re-arranging, giving

$$x = \frac{R \cos \alpha + z \sin \zeta_p}{\cos \zeta_p}. \quad (C.5)$$

The y -component is then simply given by substituting Equations C.5 into Equation C.1. Notice that because we have set the yaw of the aircraft to zero there is symmetry about the x -axis so that the intersection points of the isorange and isodop are given by $(x, \pm y, z)$. The coordinates of the points can then be transformed to the antenna frame by using Equations A.1 and A.6. The angles θ and ϕ are finally given by

$$\theta = \cos^{-1}\left(\frac{x_a}{R}\right) \quad (C.6)$$

$$\text{and } \phi = \cos^{-1}\left(\frac{y_a}{R \sin \theta}\right) \text{ or } \phi = \sin^{-1}\left(\frac{z_a}{R \sin \theta}\right) \quad (C.7)$$

as can be seen by inspection of Figure 2.1. Equations C.6 and C.7 give the angles θ and ϕ as functions of R and v , although much of the functional dependence is hidden in the expressions for the coordinates x_a , y_a and z_a .

Similarly to find expressions for the range and Doppler shift which correspond to angles θ and ϕ we express the point on the Earth's surface in spherical coordinates in the antenna frame, i.e. $\vec{r}_a = (R \cos \theta, R \sin \theta \cos \phi, R \sin \theta \sin \phi)$, and then transform to the platform frame to find the Doppler shift of the point and to the inertial frame to solve for range. Substituting into Equation A.7 and comparing expressions for the x_p -component with Equation C.3 yields

$$\cos \alpha = \cos \xi_a \cos \zeta_a \cos \theta - (\sin \xi_a \cos \phi - \cos \xi_a \sin \zeta_a \sin \phi) \sin \theta. \quad (C.8)$$

The Doppler shift of the point of the Earth's surface is then given by

$$v = 2v \cos \alpha / \lambda, \quad (C.9)$$

where v is the aircraft's velocity and λ is the wavelength of the RF carrier. Substituting the x_p and z_p coordinates of the point into the expression for the z -component from Equation A.5 yields

$$z = R \cos \gamma = -R \sin \zeta_p \cos \alpha + \cos \zeta_p (y_p \sin \zeta_p + z_p \cos \zeta_p) \quad (C.10)$$

which can then be substituted into Equation C.2 and solved for range. The resulting quadratic equations yields two solutions only one of which is physical.

Appendix D

The Response of the Radar

In essence, a pulse-Doppler radar is simply an instrument used to measure the time-frequency distribution of the environment surrounding the radar. In an APDR this is conventionally achieved by using the short-time Fourier transform to calculate the frequency distribution of the signal in a number of range bins. This is usually implemented by transmitting a regular train of pulses and taking the discrete Fourier transform of the return signal. The Woodward ambiguity function (Woodward 1980) has been used extensively in radar design and analysis to derive the performance characteristics of various waveforms used in APDRs (see e.g. Levanon 1988 and Blahut, Miller and Wilcox 1991) and is described here in detail. Two APDR waveforms are considered in this report, a simple pulse train and a thirteen-bit Barker coded pulse train, and the ambiguity functions of both waveforms are calculated in Sections D.2 and D.3. The link between radar signal processing and time frequency analysis is made in Section D.4.

D.1 Ambiguity Function Analysis

Consider a transmitted signal $s(t)$ which can be expressed in complex form as (Gabor 1946) $\psi_s(t) = s(t) - iH[s(t)]$, where $H[\]$ signifies the application of the Hilbert transform. The complex signal received from a target at range $R = c\tau/2$ due to this transmitted signal is $\psi_r(t) = a_r \psi_s(t - \tau) e^{2\pi i \nu t}$, where τ is the two-way delay to the target, ν is the Doppler shift of the target and a_r is the amplitude of the received signal. The response of a receiver consisting of a filter matched to the transmitted signal is given by

$$\chi_{rs}(\tau', \nu') = \int_{-\infty}^{\infty} \psi_r(t) \overline{\psi_s(t - \tau')} e^{-2\pi i \nu' t} dt = a_r e^{-2\pi i (\nu' - \nu) \tau} \chi_{ss}(\tau' - \tau, \nu' - \nu) \quad (D.1)$$

$$\text{where } \chi_{ss}(\tau, \nu) = \int_{-\infty}^{\infty} \psi_s(t) \overline{\psi_s(t - \tau)} e^{-2\pi i \nu t} dt, \quad (D.2)$$

is the ambiguity function of the transmitted signal and the overbar signifies the complex conjugate. We can see from Equation D.1 that the response of the receiver is simply given by a shifted version of the ambiguity function of the transmitted signal.

For example, consider a narrowband signal of the form

$$\psi_s(t) = \frac{1}{\sqrt{N}} \sum_{n=0}^{(N-1)} \mu(t - nT_r) e^{2\pi i f t}, \quad (D.3)$$

where f is the carrier frequency of the signal, T_r is the pulse repetition interval (PRI) of the pulse train, N is the total number of pulses in the pulse train and $\mu(t)$ is the envelope of the individual pulses. The ambiguity function of this signal is given by

$$\chi_{ss}(\tau, \nu) = \frac{e^{2\pi i \nu \tau}}{N} \sum_{n=0}^{(N-1)} \sum_{m=0}^{(N-1)} \chi_{\mu\mu}(\tau + (m-n)T_r, \nu) e^{-2\pi i \nu n T_r}, \quad (D.4)$$

$$\text{where } \chi_{\mu\mu}(\tau, \nu) = \int_{-\infty}^{\infty} \mu(t) \overline{\mu(t-\tau)} e^{-2\pi i \nu t} dt, \quad (D.5)$$

is the ambiguity function of the individual pulses in the pulse train. The response of an ideal matched receiver to a pulse train can be seen from Equation D.4 to consist of two components. The inner summation yields the range response of the radar and is simply a pulse train formed from the ambiguity function of the individual pulses. The outer summation is in the form of a discrete Fourier transform and produces the Doppler response of the radar. The response of the receiver to this pulse train is then given by substituting Equation D.4 into Equation D.1.

In this example the receiver has been matched to the transmitted signal. This is done because the matched filter is optimal in the sense that it maximises the signal to noise ratio of the receiver. However the Doppler response of the filter is poor and has unacceptably high sidelobes. Hence in practice the received signal is generally compared with a filter consisting of a weighted pulse train of the form

$$\psi_f(t) = \frac{1}{\sqrt{N}} \sum_{n=0}^{(N-1)} w_n \mu'(t - nT_r) e^{2\pi i f t}, \quad (D.6)$$

where w_n is the weighting of the n^{th} pulse and $\mu'(t)$ is the envelope of the individual pulses, not necessarily the same as the envelope of the transmitted pulses. The response of the receiver is now given by

$$\chi_{rf}(\tau', \nu') = a_r e^{-2\pi i (\nu' - \nu) \tau} \chi_{sf}(\tau' - \tau, \nu' - \nu) \quad (D.7)$$

$$\text{where } \chi_{sf}(\tau, \nu) = \int_{-\infty}^{\infty} \psi_s(t) \overline{\psi_f(t-\tau)} e^{-2\pi i \nu t} dt \quad (D.8)$$

is the cross ambiguity function of the transmitted signal and the filter signal.

D.2 Simple Pulse Train

Consider a simple pulse train (Equation D.3) which has an envelope given by

$$\mu(t) = \frac{1}{\sqrt{T_p}} \text{rect}\left(\frac{t}{T_p}\right), \quad (\text{D.9})$$

$$\text{where } \text{rect}(t) = \begin{cases} 1, & 0 \leq t \leq 1 \\ 0, & \text{otherwise} \end{cases}$$

and T_p is the pulse duration.

Consider also a receiver with a weighted matched filter given by Equation D.6 with $\mu'(t) = \mu(t)$. The resulting cross ambiguity function (Equation D.8) is given by

$$\chi_{sf}(\tau, \nu) = \frac{e^{2\pi i \nu \tau}}{N} \sum_{n=0}^{(N-1)} \sum_{m=0}^{(N-1)} \bar{w}_m \chi_{\mu\mu}(\tau + (m-n)T_r, \nu) e^{-2\pi i \nu m T_r}. \quad (\text{D.10})$$

Since the duty cycle of the pulse train is much less than 50% it is possible to re-write Equation D.10 as

$$\chi_{sf}(\tau, \nu) = \frac{e^{2\pi i \nu (\tau - kT_r)}}{N} \chi_{\mu\mu}(\tau + kT_r, \nu) \sum_{n=0}^{(N-1)} \bar{w}_n e^{-2\pi i \nu n T_r}, \quad (\text{D.11})$$

where $k = \text{int}(-\tau/T_r)$ and we have used the fact that discrete Fourier Transform is circular. We can calculate $\chi_{\mu\mu}(\tau, \nu)$ by substituting Equation D.9 into D.5 yielding

$$\chi_{\mu\mu}(\tau, \nu) = \frac{1}{T_p} \int_{t_{\min}}^{t_{\max}} e^{-2\pi i \nu t} dt, \quad (\text{D.12})$$

$$\text{where } t_{\min} = \begin{cases} 0, & -T_p \leq \tau \leq 0 \\ \tau, & 0 \leq \tau \leq T_p \end{cases} \text{ and } t_{\max} = \begin{cases} \tau + T_p, & -T_p \leq \tau \leq 0 \\ T_p, & 0 \leq \tau \leq T_p \end{cases}.$$

For radar applications the Doppler shift of the return is generally much less than the bandwidth of the receiver, i.e. $\nu T_p \ll 1$, and hence we can make the approximation

$$\chi_{\mu\mu}(\tau, \nu) \approx \frac{1}{T_p} \int_{t_{\min}}^{t_{\max}} dt = \begin{cases} 1 - \frac{|\tau|}{T_p}, & \text{for } -T_p \leq \tau \leq T_p \\ 0, & \text{otherwise} \end{cases}. \quad (\text{D.13})$$

The ambiguity function for a rectangular pulse with a duration of $T_p = 1 \mu\text{s}$ is shown in Figure D.1. From this example we can see that the central peak of the ambiguity function is relatively short in the delay domain but relatively broad in the Doppler domain. Hence for APDR applications where the maximum Doppler shifts experienced are in the order of tens of kilohertz, we can make the approximation that the ambiguity function is independent of Doppler shift, i.e. $\chi_{\mu\mu}(\tau, \nu) \approx \chi_{\mu\mu}(\tau)$. From Figure D.1 we can also see that the range response of the radar is given by the autocorrelation of the individual pulses.

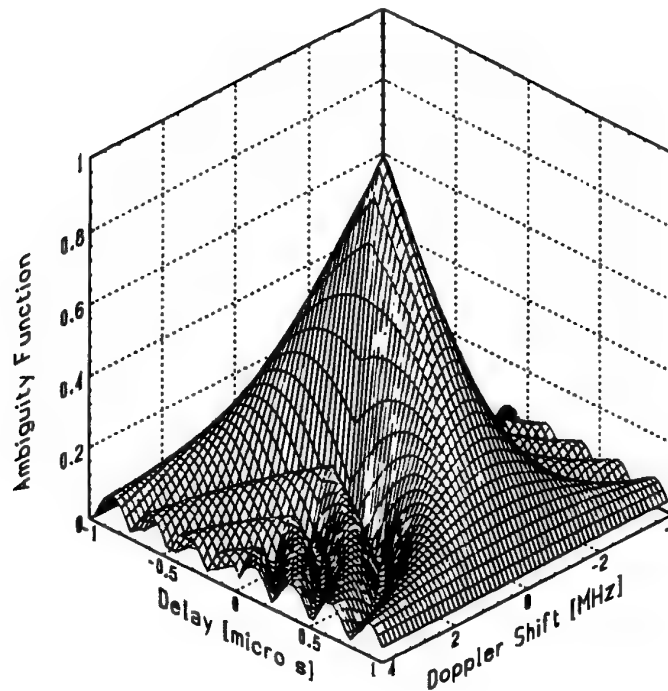


Figure D.1 The ambiguity function, $\chi_{\mu\mu}(\tau, \nu)$, of a rectangular pulse with a duration of $1 \mu\text{s}$.

The cross ambiguity function for a train of rectangular pulses and a Dolph-Chebyshev weighted matched filter (Equation D.11) is shown in Figure D.2. The Dolph-Chebyshev weights are calculated as described in Appendix E and are chosen so that the frequency response of the filter has uniform sidelobes which are 55 dB down from the mainlobe. Here the PRI is given by $T_r = N_{rb}T_p$ where $N_{rb} = 64$ is the number of range bins formed and $N = 32$ is the number of Doppler filters formed.

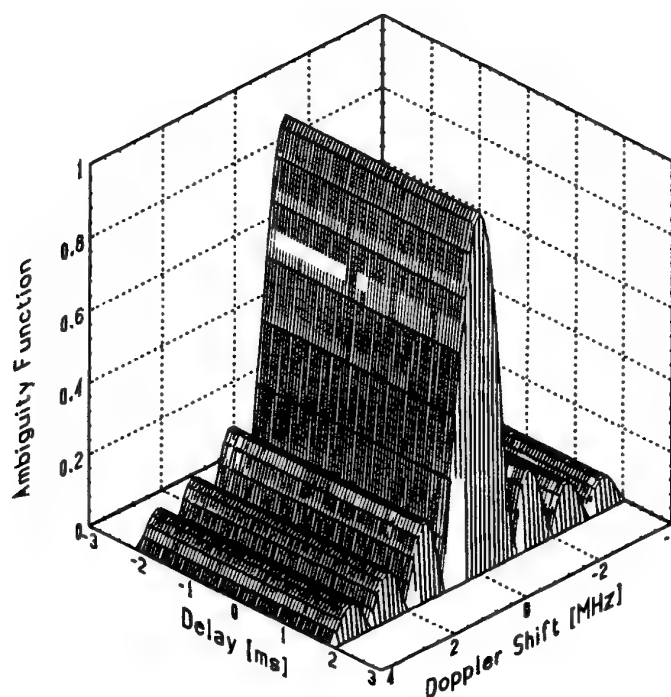


Figure D.2 The cross ambiguity function, $\chi_{sf}(\tau, \nu)$, of a simple pulse train and a Dolph-Chebyshev weighted matched filter. Here we have used a PRI of $64 \mu\text{s}$ which corresponds to a PRF of 15.625 kHz and we have generated 32 Doppler filters.

While the ambiguity function looks smooth in Figure D.2, it is in fact composed of a grid of spikes. The spikes are spaced by the PRI in delay and by the PRF in Doppler shift. The spacing of the spikes indicates the degree of ambiguity in the waveform and for an MPRF APDR the waveform is ambiguous in both range and Doppler shift. The region around $\tau = 0$ and $\nu = 0$ is shown in more detail in Figure D.3. Here we can clearly see the uniform sidelobes produced by the Dolph-Chebyshev weighting. The dimensions of the central peak indicate the range-Doppler resolution of the waveform, and in this case we have a range resolution of approximately 150 metres and a Doppler resolution of approximately 500 Hz.

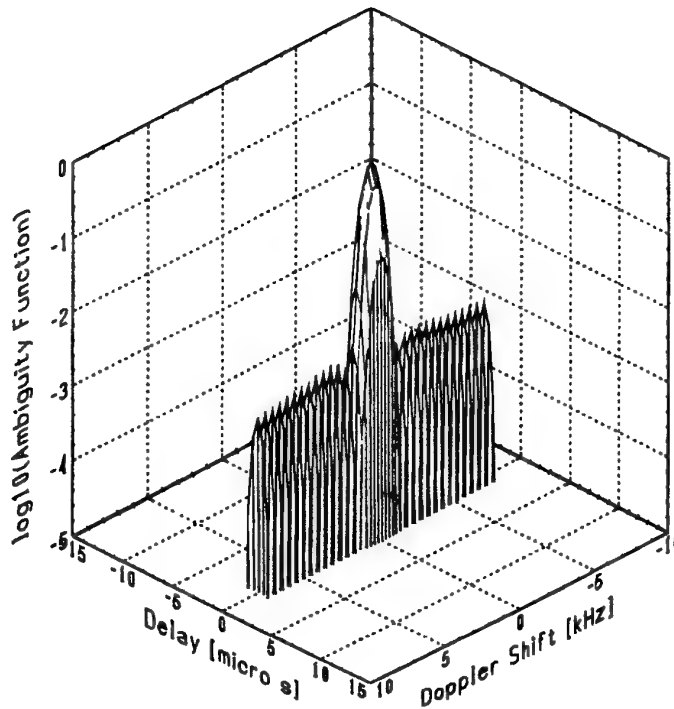


Figure D.3 A close up in the region near $\tau = 0$ and $\nu = 0$ of the cross ambiguity function shown in Figure D.2.

The matched filter described above is an ideal case. In practice the matched filter is often approximated by a low pass filter with an impulse response

$$\mu'(t) = \sqrt{\frac{2}{T_p}} e^{-t/T_p}, \quad (D.14)$$

for $t > 0$. The low pass filter is used because it is simple to implement and offers a reasonable approximation to the matched filter. The cross ambiguity function for a receiver employing a Dolph-Chebyshev weighted, low pass filter is given by

$$\chi_{sf}(\tau, \nu) = \frac{e^{2\pi i \nu (\tau - kT_r)}}{N} \chi_{\mu\mu'}(\tau + kT_r, \nu) \sum_{n=0}^{(N-1)} \bar{w}_n e^{-2\pi i \nu n T_r}, \quad (D.15)$$

$$\text{where } \chi_{\mu\mu'}(\tau, \nu) = \int_{-\infty}^{\infty} \mu(t) \overline{\mu'(t - \tau)} e^{-2\pi i \nu t} dt. \quad (D.16)$$

Substituting Equations D.9 and D.14 into Equation D.16 we can again approximate the ambiguity function by

$$\chi_{\mu\mu'}(\tau, \nu) = \frac{1}{T_p} \int_{t_{\min}}^{t_{\max}} \sqrt{2} e^{-(t-\tau)/T_p} e^{-2\pi i \nu \tau} dt \approx \sqrt{2} e^{\tau/T_p} \left[e^{-\max(\tau, 0)/T_p} - e^{-1} \right]. \quad (\text{D.17})$$

The effect low pass filter has on the cross ambiguity function can be seen from Figure D.4 where we have plotted the cross ambiguity function in the region near $\tau = 0$ and $\nu = 0$. The cross ambiguity function is now asymmetric in delay and has a tail extending several microseconds.

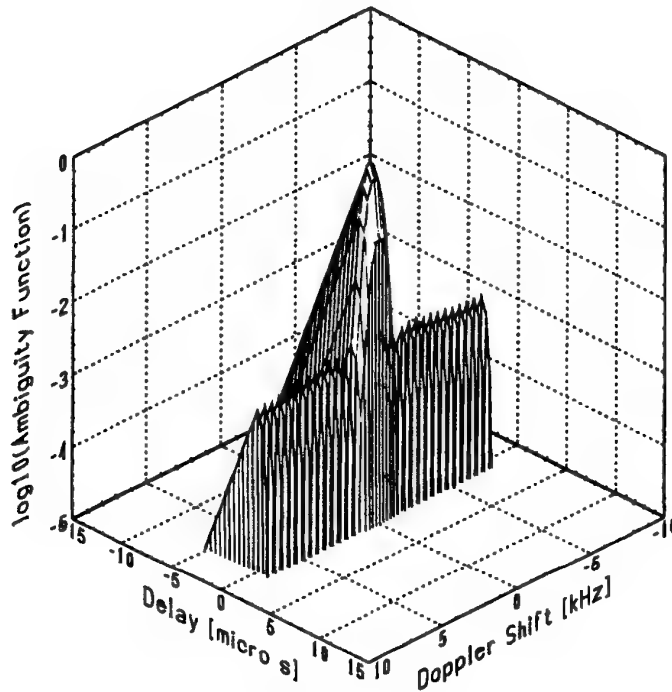


Figure D.4 A close up of the cross ambiguity function in the region near $\tau = 0$ and $\nu = 0$ for a simple pulse train and a Dolph-Chebyshev weighted low pass filter. Again we have $T_p = 1 \mu\text{s}$, $T_r = 64 \mu\text{s}$ and $N = 32$.

D.3 13-Bit Barker Coded Pulse Train

Consider a thirteen bit Barker coded transmitted waveform given by

$$\psi_s(t) = \frac{1}{\sqrt{13N}} \sum_{n=0}^{(N-1)} \sum_{m=0}^{12} \mu(t - nT_r - mT_p) e^{i\phi_m} e^{2\pi i f t}, \quad (\text{D.18})$$

where $\mu(t)$ is given by Equation D.9, T_p is now the duration of the Barker bits and the phase coding is given by the first exponential with $\phi_m = 0, 0, 0, 0, 0, \pi, \pi, 0, 0, \pi, 0, \pi, 0$ for $m = 0, \dots, 12$. Barker coded waveforms are used to increase the duty cycle of the radar, while maintaining the range resolution. As shall be seen, the cost of using such a waveform is the introduction of sidelobes in the range response of the radar.

Consider a weighted matched filter of the form

$$\psi_f(t) = \frac{1}{\sqrt{13N}} \sum_{n=0}^{(N-1)} w_n \sum_{m=0}^{12} \mu(t - nT_r - mT_p) e^{i\phi_m} e^{2\pi i f t}. \quad (\text{D.19})$$

The resulting cross ambiguity function is given by

$$\chi_{sf}(\tau, \nu) = \frac{e^{2\pi i \nu \tau}}{13N} \sum_{n_1=0}^{(N-1)} \sum_{n_2=0}^{(N-1)} \bar{w}_{n_2} \sum_{m_1=0}^{12} \sum_{m_2=0}^{12} \chi_{\mu\mu}(\tau + (n_2 - n_1)T_r + (m_2 - m_1)T_p, \nu) \times e^{i(\phi_{m_1} - \phi_{m_2})} e^{-2\pi i \nu (n_1 T_r + m_1 T_p)}. \quad (\text{D.20})$$

For radar applications, Equation D.20 can be simplified to give (c.f. Equation D.11)

$$\chi_{sf}(\tau, \nu) = \frac{e^{2\pi i \nu (\tau - kT_r)}}{13N} \sum_{n=0}^{(N-1)} \bar{w}_n e^{-2\pi i \nu n T_r} \sum_{m_1=0}^{12} e^{-2\pi i \nu m_1 T_p} \sum_{m_2=m_2^{\min}}^{m_2^{\max}} \chi_{\mu\mu}(\tau + kT_r + (m_2 - m_1)T_p, \nu) e^{i(\phi_{m_1} - \phi_{m_2})} \quad (\text{D.21})$$

$$\text{where } m_2^{\min} = \max(0, \text{int}(-(\tau + kT_r)/T_p) + m_1 - 1), \quad (\text{D.22})$$

$$m_2^{\max} = \min(12, \text{int}(-(\tau + kT_r)/T_p) + m_1 + 1), \quad (\text{D.23})$$

and $\chi_{\mu\mu}(\tau, \nu)$ is given by Equation D.13.

The cross ambiguity function which results for $T_p = 1 \mu\text{s}$, $T_r = N_{rb} T_p$, $N_{rb} = 64$ and $N = 32$ is shown in Figure D.5. The Doppler response is identical to that for the simple pulse train, however the phase coding has introduced sidelobes in delay which extend thirteen microseconds either side of the peak.

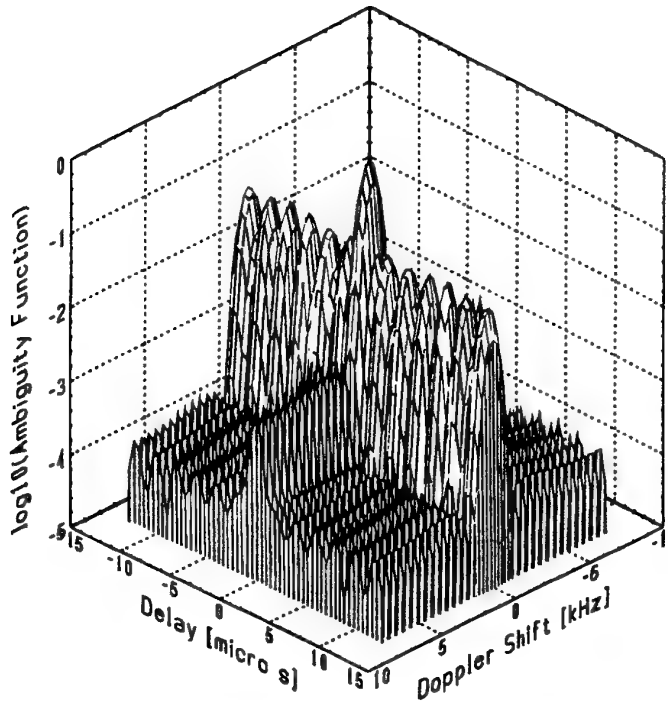


Figure D.5 A close up of the cross ambiguity function in the region near $\tau = 0$ and $\nu = 0$ for a thirteen bit Barker coded pulse train and a Dolph-Chebyshev weighted matched filter. Again we have $T_p = 1 \mu s$, $T_r = 64 \mu s$ and $N = 32$.

If we again consider the case where the matched filter has been realised by a low pass filter then the resulting cross ambiguity function is given by

$$\chi_{sf}(\tau, \nu) = \frac{e^{2\pi i \nu \tau}}{13N} \sum_{n_1=0}^{(N-1)} \sum_{n_2=0}^{(N-1)} \bar{w}_{n_2} \sum_{m_1=0}^{12} \sum_{m_2=0}^{12} \chi_{\mu\mu'}(\tau + (n_2 - n_1)T_r + (m_2 - m_1)T_p, \nu) \times e^{i(\phi_{m_1} - \phi_{m_2})} e^{-2\pi i \nu (n_1 T_r + m_1 T_p)} \quad (D.24)$$

For radar applications Equation D.24 can again be simplified to give (c.f. Equation D.11)

$$\chi_{sf}(\tau, \nu) = \frac{e^{2\pi i \nu (\tau - kT_r)}}{13N} \sum_{n=0}^{(N-1)} \bar{w}_n e^{-2\pi i \nu n T_r} \sum_{m_1=0}^{12} e^{-2\pi i \nu m_1 T_p} \sum_{m_2=0}^{m_2^{\max}} \chi_{\mu\mu'}(\tau + kT_r + (m_2 - m_1)T_p, \nu) e^{i(\phi_{m_1} - \phi_{m_2})} \quad (D.25)$$

where m_2^{\max} is given by Equation D.23 and $\chi_{\mu\mu'}(\tau, \nu)$ is given by Equation D.17.

The cross ambiguity function which results when a Dolph-Chebyshev weight low pass filter is used in conjunction with Barker coding is shown in Figure D.6.

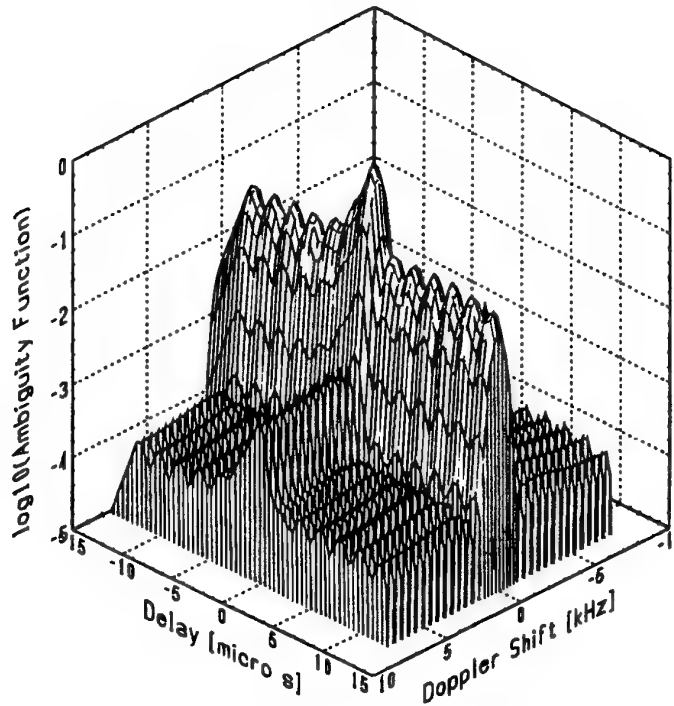


Figure D.6 A close up of the cross ambiguity function in the region near $\tau = 0$ and $\nu = 0$ for a thirteen bit Barker coded pulse train and a Dolph-Chebyshev weighted low pass filter. Again we have $T_p = 1 \mu s$, $T_r = 64 \mu s$ and $N = 32$.

D.4 Time-Frequency Analysis

The principal aim of time-frequency analysis is to derive a distribution which describes the energy density of a signal as a function of *both* time and frequency. Such a distribution enables us to characterise signals such as speech whose spectral content is changing with time. It can be shown that an infinite number of possible distributions exist (see e.g. Cohen 1989), however we will restrict ourselves to the Rihaczek distribution (Rihaczek 1969). The Rihaczek distribution of a signal $\psi(t)$ with spectral density $\Psi(f)$ is defined as

$$I(t, f) = \psi(t) \overline{\Psi(f)} e^{-2\pi i f t}. \quad (D.26)$$

The symbol I has been used here because the Rihaczek distribution gives the intensity of the signal, i.e. the energy per unit time, per unit frequency. The total energy of the signal is given by

$$E = \int_{-\infty}^{\infty} \int_{-\infty}^{\infty} I(t, f) dt df. \quad (D.26)$$

with the marginals giving the time and frequency energy densities of the signal, i.e. $\int I(t, f) dt = |\Psi(f)|^2$ and $\int I(t, f) df = |\psi(t)|^2$. The Rihaczek distribution is interesting in the context of this report as it may be generated by taking the two dimensional Fourier transform of the ambiguity function,

$$I(t, f) = \int_{-\infty}^{\infty} \int_{-\infty}^{\infty} \chi(\tau, \nu) e^{2\pi i(t\nu - \tau f)} d\tau d\nu = \int_{-\infty}^{\infty} \int_{-\infty}^{\infty} \int_{-\infty}^{\infty} \psi(u) \overline{\psi(u - \tau)} e^{2\pi i(v(t-u) - \tau f)} du d\tau dv. \quad (D.28)$$

For example, the Rihaczek distribution for the simple pulse train and a Dolph-Chebyshev weighted matched filter (shown in Figure D.3) is given by

$$I_{sf}(t, f) = \frac{1}{N} \overline{M(f - f_o)} e^{-2\pi i(f - f_o)t} \sum_{n=0}^{(N-1)} w_n e^{2\pi i(f - f_o)nT_r} \sum_{m=0}^{(N-1)} \mu(t - mT_r). \quad (D.29)$$

$$\text{where } M(f) = \int_{-\infty}^{\infty} \mu(t) e^{-2\pi i f t} dt. \quad (D.30)$$

For a reviews of time-frequency analysis see Cohen (1989) and Boashash (1992).

Appendix E

Dolph-Chebyshev Weighting

This appendix has been included because the description of Dolph-Chebyshev weighting provided in Harris (1978) requires some clarification. Harris presents the Fourier transform of the Dolph-Chebyshev weights for a data window, however he does not make it clear that the formula only apply for an odd number of window elements. That is remedied here by presenting formula for both even and odd numbers of elements. Consider an N element window. The Fourier transform of the weights is given by

$$A_k = \frac{T_m(u_o \cos(\pi k/2n))}{T_m(u_o)}, \quad (\text{E.1})$$

where $k = -n, \dots, -1, 0, 1, \dots, n$ if $N = 2n + 1$ is odd, and $k = -(n - 1), \dots, -1, 0, 1, \dots, n$ if $N = 2n$ is even. Here

$$T_m(u) = \begin{cases} \cos(m \cos^{-1} u), & \text{for } -1 \leq u \leq 1 \\ \cosh(m \cosh^{-1} u), & \text{for } |u| > 1 \end{cases} \quad (\text{E.2})$$

is a Chebyshev polynomial of degree $m = (N - 1)$ and u_o is given by

$$u_o = \cosh(m^{-1} \cosh^{-1} b). \quad (\text{E.3})$$

where b is the desired sidelobe ratio. The Dolph-Chebyshev weights are then simply given by taking the DFT of Equation E.1.

DSTO-TR-0323

A Theoretical Analysis of Target Tracking in Ground Clutter by
Airborne Pulse Doppler Radars

A. P. Szabo

DSTO-TR-0323

AUSTRALIA

1. DEFENCE ORGANISATION

a. Task sponsor: DGFD (AEROSPACE) Att EW1

b. S&T Program

Chief Defence Scientist	} shared copy
FAS Science Policy	
AS Science and Industry Interaction	
AS Science Corporate Management	
Counsellor Defence Science, London	(Doc Data Sheet)
Counsellor Defence Science, Washington	
Scientific Adviser to MRDC, Thailand	(Doc Data Sheet)
Senior Defence Scientific Adviser/Scientific Adviser Policy and Command	
(shared copy)	
Navy Scientific Adviser	
(3 copies Doc Data Sheet and one copy of the distribution list)	
Scientific Adviser - Army	(Doc Data Sheet and distribution list)
Air Force Scientific Adviser	
Director Trials	

Electronics and Surveillance Research Laboratory

Chief of Electronic Warfare Division
Research Leader. Electronic Countermeasures
Head, Electronic Countermeasures Group
Task Manager: Dr. T. Winchester, Electronic Warfare Division
Head, Vulnerability Assessment Group
Dr. A.P. Szabo, Electronic Countermeasures Group
Dr. D. Bucco, Guided Weapons Division
Dr. J. Whitrow, Microwave Radar Division
Dr. R. Hawkes, Microwave Radar Division

DSTO Library

Library Fishermens Bend	
Library Maribyrnong	
Library DSTOS	(2 copies)
Library, MOD, Pyrmont (Doc Data)	

c. Forces Executive

Director General Force Development (Sea)	(Doc Data Sheet)
Director General Force Development (Land)	(Doc Data Sheet)
Director General Force Development (Air)	

d. Navy

e. Army

ABCA Office, G-1-34, Russell Offices, Canberra	(4 copies)
--	------------

- f. **Air Force**
No compulsory distribution
- g. **S&I Program**
Defence Intelligence Organisation
Library, Defence Signals Directorate (Doc Data Sheet)
- h. **Acquisition and Logistics Program**
No compulsory distribution
- i. **B&M Program (libraries)**
OIC TRS, Defence Central Library
Officer in Charge, Document Exchange Centre (DEC)
DEC requires the following copies of public release reports to meet exchange agreements under their management:
 - US Defense Technical Information Center, 2 copies
 - UK Defence Research Information Centre, 2 copies
 - Canada Defence Scientific Information Service
 - NZ Defence Information Centre
 - National Library of Australia
- 2. **UNIVERSITIES AND COLLEGES**
Australian Defence Force Academy
Library
Head of Aerospace and Mechanical Engineering
Deakin University, Serials Section (M list), Deakin University Library,
Geelong, 3217, (Research and Technical Reports only)
Senior Librarian, Hargrave Library, Monash University
Librarian, Flinders University
- 3. **OTHER ORGANISATIONS**
NASA (Canberra)
AGPS
State Library of South Australia
Parliamentary Library, South Australia

OUTSIDE AUSTRALIA

- 4. **ABSTRACTING AND INFORMATION ORGANISATIONS**
INSPEC: Acquisitions Section Institution of Electrical Engineers
Library, Chemical Abstracts Reference Service
Engineering Societies Library, US
American Society for Metals
Documents Librarian, The Center for Research Libraries, US
- 5. **INFORMATION EXCHANGE AGREEMENT PARTNERS**
Acquisitions Unit, Science Reference and Information Service, UK
Library - Exchange Desk, National Institute of Standards and Technology, US
National Aerospace Laboratory, Japan
National Aerospace Laboratory, Netherlands

SPARES (10 copies)

Total number of copies: 62

DOCUMENT CONTROL DATA SHEET

1. Page Classification
UNCLASSIFIED
2. Privacy Marking/Caveat

3a. AR Number AR-009-664	3b. Establishment Number DSTO-TR-0323	3c. Type of Report TECHNICAL REPORT	4. Task Number ADA 94/352
5. Document Date JUNE 1996	6. Cost Code 823707	7. Security Classification <input type="checkbox"/> U <input type="checkbox"/> U <input type="checkbox"/> U	8. No. of Pages 78
10. Title A Theoretical Analysis of Target Tracking in Ground Clutter by Airborne Pulse Doppler Radars		9. No. of Refs. 23	
11. Author(s) A. P. Szabo		12. Downgrading/ Delimiting Instructions No limitation	
13a. Corporate Author and Address Electronic Warfare Division Electronics and Surveillance Research Laboratory PO Box 1500 SALISBURY SA 5108		14. Officer/Position responsible for Security SOESRL Downgrading CEWD Approval for release CEWD	
13b. Task Sponsor DGFD (AEROSPACE)			
15. Secondary Release Statement of this Document APPROVED FOR PUBLIC RELEASE. <small>Any enquiries outside stated limitations should be referred through DSTIC, Defence Information Services, Department of Defence, Anzac Park West, Canberra, ACT 2600.</small>			
16a. Deliberate Announcement No limitation.			
16b. Casual Announcement (for citation in other documents) <input checked="" type="checkbox"/> No Limitation <input type="checkbox"/> Ref. by Author, Doc No and date only			
17. DEFTEST Descriptors Ground clutter Airborne radar Models Radar tracking Random noise Radar signals Pulse Doppler radar Repetition rate Frequency analyzers			18. DISCAT Subject Codes
19. Abstract Target tracking in ground clutter is an important function of airborne pulse Doppler radars. As a tool for analysing the performance of these radars, modifications to an existing computer model of the medium pulse repetition frequency signal target track mode of an airborne radar have been made to include ground clutter. The clutter signal has been modelled as a Gaussian random field with uncorrelated increments. The field is characterised by the mean clutter power and examples of the mean clutter power are shown for straight-and-level and diving aircraft. A method of sampling a realisation of the clutter signal in the range-Doppler bins of the radar receiver is described. Examples of the clutter signal are shown for receivers utilising Dolph-Chebyshev weighted Doppler filters and simple pulse train or thirteen bit Barker coded waveforms. Pulse repetition frequency selection in single target track mode is considered in detail. Examples of the output from the computer model, both with and without clutter included, are also presented. The results of this analysis show that ground clutter has a significant impact on the way in which single target track mode is implemented and needs to be included to accurately model the performance of the radar.			